TOPICAL REVIEW

Strong-field rescattering physics—self-imaging of a molecule by its own electrons

C D Lin[1]**, Anh-Thu Le**[1]**, Zhangjin Chen**[1]**, Toru Morishita**[2,3] **and Robert Lucchese**[4]

[1] J. R. Macdonald Laboratory, Physics Department, Kansas State University, Manhattan, KS 66506-2604, USA

[2] Department of Applied Physics and Chemistry, University of Electro-Communications, 1-5-1 Chofu-ga-oka, Chofu-shi, Tokyo, 182-8585, Japan

[3] PRESTO, Japan Science and Technology Agency, Kawaguchi, Saitama 332-0012, Japan

[4] Department of Chemistry, Texas A&M University, College Station, TX 77843-3255, USA

E-mail: cdlin@phys-ksu.edu

Abstract

When an atom or molecule is exposed to a short intense laser pulse, electrons that were removed at an earlier time may be driven back by the oscillating electric field of the laser to recollide with the parent ion, to incur processes like high-order harmonic generation (HHG), high-energy above-threshold ionization (HATI) and nonsequential double ionization (NSDI). Over the years, a rescattering model (the three-step model) has been used to understand these strong field phenomena qualitatively, but not quantitatively. Recently we have established such a quantitative rescattering (QRS) theory. According to QRS, the yields for HHG, HATI and NSDI can be expressed as the product of a returning electron wave packet with various *field-free* electron–ion scattering cross sections, namely photo-recombination, elastic electron scattering and electron-impact ionization, respectively. The validity of QRS is first demonstrated by comparing with accurate numerical results from solving the time-dependent Schrödinger equation (TDSE) for atoms. It is then applied to atoms and molecules to explain recent experimental data. According to QRS, accurate *field-free* electron scattering and photoionization cross sections can be obtained from the HATI and HHG spectra, respectively. These cross sections are the conventional tools for studying the structure of a molecule; thus, QRS serves to provide the required theoretical foundation for the self-imaging of a molecule in strong fields by its own electrons. Since infrared lasers of duration of a few femtoseconds are readily available today, these results imply that they are suitable for probing the dynamics of molecules with temporal resolutions of a few femtoseconds.

(Some figures in this article are in colour only in the electronic version)

1. Introduction

1.1. Strong-field physics and the rescattering phenomena

When an atom or molecule is exposed to an intense short infrared laser pulse, an electron that was ejected at an earlier time may be driven back by the oscillating electric field to revisit its parent ion. Such an encounter, or rescattering, may lead to a number of different electron–target ion collisional phenomena. Among them the best-known and most-studied is high-order harmonic generation (HHG) [1–3]. These high-order harmonics have been manipulated to produce extreme

ultraviolet (XUV) attosecond pulses or attosecond pulse trains [4, 5]. There are also other rescattering phenomena—e.g. the generation of high-energy above-threshold-ionization (HATI) electrons [6, 7], and nonsequential double ionization (NSDI) of atoms and molecules [8–10]. All of these processes may be qualitatively understood as the result of collisions between a returning electron wave packet and the target ion, analogous to collisions between a beam of laboratory-prepared electrons and the target ion. Thus, HHG is the recombination of the returning electrons with the target ion, with the emission of high-energy photons, while HATI electrons are from the elastic scattering of the returning electrons in the backward directions by the ion [11, 12]. Furthermore, NSDI occurs when the returning electron knocks out another electron from the target ion, analogous to the (e, 2e) process. Both electron scattering and photoionization are the conventional means for probing the structure of atoms and molecules. Thus HHG, HATI and NSDI offer potentially powerful tools for revealing the structure of the target. Today, infrared laser pulses with durations of a few femtoseconds are readily available; thus, these rescattering processes may be used to investigate the transient structure of molecules, with temporal resolution of a few femtoseconds [13].

1.2. Probing molecular structure with strong fields

The potential for probing the structure of a molecule with infrared lasers has been discussed widely since the 1990s. For a review on these earlier works, see [14]. For example, theoretical calculations have shown that laser-induced electron diffraction (LIED) spectra exhibit clear diffraction minima for H_2^+ [15] and K_2^+ [16] in the angle-resolved photoelectrons. However, these calculations were carried out at large interatomic separations, on the order of 10–20 au. In LIED, diffraction occurs in the presence of the laser field. To isolate the structure information, distortions of the diffraction images due to the laser field have to be removed [17, 18]. In a typical experiment, the laser field is not known very precisely, such that it would also limit the retrieval of the structural information. Thus, in spite of its promise, LIED has not made much progress in actual applications so far.

An alternative route for uncovering the structure of a molecule is through laser-induced HHG spectra. In a 2004 *Nature* paper, Itatani *et al* [19] reported that they reconstructed the highest occupied molecular orbital (HOMO) of N_2 molecules accurately from the alignment-dependent HHG spectra using the tomographic procedure. That paper has generated a great deal of interest. However, the tomographic procedure assumes that the continuum wavefunction of the electron in the recombination process can be represented by a plane wave [19, 20]. In molecular physics, it is well known that this is a severe approximation. Using plane waves, interesting phenomena in the photoionization of molecules such as resonances and non-monotonic energy dependence of cross sections would have been completely missed. Alternatively, if the continuum electrons can be described by plane waves, then HHG spectra from molecules would have been easily calculated [21]. In quantum chemistry,

the ground state wavefunction of a molecule can be quite accurately computed by packages such as GAMESS [22], GAUSSIAN [23] and MOLPRO [24]. The difficulty of treating HHG or HATI lies in the calculation of continuum wavefunctions.

The major roadblock to extracting accurate structural information using LIED or HHG lies in the fact that laser-induced photoelectron spectra or high-order harmonics occur via nonlinear processes. Except for very simple systems, there exist no established theoretical tools such that accurate HATI or HHG spectra can be efficiently calculated. Unlike conventional x-ray diffraction, where the diffraction pattern in the far field is the Fourier transform of the object [25, 26], no such simple relation exists in HATI or HHG. Before structural information of a molecule can be extracted from laser-generated electron or photon spectra, accurate theories of HATI and HHG for molecules first have to be established. Since structural retrieval is an inverse scattering problem, it is desirable that the scattering theory of HATI and HHG be relatively simple. Brute-force and complicated numerical solution of the time-dependent Schrödinger equation (TDSE) of a many-electron molecular system clearly cannot be the answer.

1.3. Quantitative rescattering (QRS) theory—a qualitative description

Our approach to discovering a simple theory for HATI and HHG phenomena is to build upon the rescattering concept. According to this model, electrons are first tunnel-ionized at an early time of the laser pulse. They are then accelerated by the laser field and some may be thrown back to recollide with the target ion. Can these returning electrons be represented by an electron wave packet (EWP), $W(k_r)$, similar to a beam of free electrons prepared in the laboratory? The answer is not obvious. The rescattering model is based on a classical or semiclassical concept [27]. Without including the effect of the target potential, a classical calculation shows that the maximum returning kinetic energy is $3.2U_p$, where U_p is the ponderomotive energy, $U_p = I/4\omega^2$, with ω the angular frequency of the laser and I the peak intensity. (In this review, atomic units are used, and lasers are linearly polarized, unless otherwise noted.) For HHG, the returning kinetic energy is converted to photon energy such that the HHG cutoff is given by $3.2U_p + I_p$, where I_p is the ionization energy. For HATI electrons, the elastically scattered electrons gain an additional linear momentum, $-A(t_r)$, along the laser polarization axis, as they leave the laser field. Here $A(t_r)$ is the vector potential at the time of recollision, t_r. Thus the cutoff is at about $10U_p$ if the electrons are backscattered by 180° [28]. These classical predictions, while being supported by experimental data, are by no means 'exact' since the cutoff of HHG or HATI spectra in general cannot be precisely identified.

The above observations have been known since the early 1990s [6]. Unfortunately, such a rescattering model offers no means for carrying out actual calculations, except, perhaps, within the strong-field approximation (SFA) [27, 29–31]. However, HHG and HATI spectra calculated using the SFA agree with experiments only qualitatively in general [32],

even though some features predicted from the SFA are quite adequate (more on this later). To cast the rescattering model in a quantitative form, the classical model is not enough since the EWP should be a complex function (i.e. a coherent electron beam) and electron–ion collisions should be treated quantum mechanically. Indeed, attempts have been made to extract $W(k_r)$ from the solution of the time-dependent Schrödinger equation (TDSE) [33]. To do so, there are two difficulties. First, the returning EWP is small in comparison to the total wavefunction. Second, the wavefunctions from the TDSE are calculated in general in coordinate space. In the laser field, depending on the gauge used, the kinetic momentum k_r is not a conjugate variable to the spatial coordinate in general. Thus, a quantum EWP in the rescattering model has never been successfully extracted from TDSE calculation.

In the last two years we have re-examined the rescattering model with the aim of making it into a practical theory that can be used for quantitative predictions. To build such a theory we started with a model one-electron atomic system where we can solve the TDSE to obtain HATI and HHG spectra accurately [34]. For such a simple system we also can solve field-free elastic scattering differential cross sections (DCS) and photo-recombination cross sections (PRCS) 'exactly'. Based on the rescattering concept, we then *define* an EWP, $W(k_r)$, taken to be the ratio of the HATI yield with respect to the elastic DCS. By doing so, we found that the resulting EWPs obtained for different targets are essentially identical if they are subject to identical laser pulses [32, 34]. Moreover we can define a similar $W(k_r)$, if the HATI spectra are calculated using the SFA and the elastic DCS are calculated by approximating the continuum electrons by plane waves (to be consistent with the SFA). The $W(k_r)$ thus obtained from the TDSE and from the SFA have nearly identical dependence on k_r—they differ only by an overall normalization. The latter simply reflects the fact that the total ionization rate predicted by the SFA is not correct.

The good agreement of $W(k_r)$ obtained from the SFA and TDSE has a significant consequence. Since numerical calculation of the SFA is many thousands times faster than solving the TDSE directly, we proposed a quantitative rescattering (QRS) theory where the HATI spectra are obtained as the product of a $W(k_r)$ calculated from the SFA with the accurate field-free electron–ion scattering DCS [35]. Since $W(k_r)$ does not depend on the target, it can be obtained from any simple target system. The field-free DCS can be obtained from computational packages for electron–atom or electron–molecule collisions developed over the past five decades. In a similar fashion, such a theory can be extended to HHG [36] as well as to NSDI [37] where the collisional process with the target ion is photo-recombination and electron-impact ionization, respectively. With QRS, we thus have a very simple theory to make quantitative predictions on strong-field rescattering phenomena. We remark that the calculations are based on quantum mechanical theory; thus, QRS actually can be applied at the level of complex scattering amplitudes, such that one can define a complex electron wave packet, i.e. a coherent electron wave packet. The latter will be addressed when we discuss QRS for HHG. For the time being we will concentrate only on cross sections and yields.

1.4. The significance of QRS on strong-field physics and imaging

Based on QRS, the quantum theory of rescattering phenomena becomes very simple and QRS can be used to make quantitative calculations to compare with experimental results. This has not always been possible in strong-field physics. There are three reasons. First, performing a theoretical calculation for each laser intensity is already quite time consuming. To compare with experiments, repetitive calculations must be carried out over hundreds of intensities in order to account for the contributions from all the intensities within the laser focal volume. Second, the yields for the rescattering phenomena are small and high-precision calculations for complex systems are difficult to achieve in general. Third, in a given experiment, the laser peak intensity and some other parameters are not always accurately determined. Using QRS, these problems should not be as severe. For each new laser intensity, or new wavelength, according to QRS, one only needs to calculate the new EWP, $W(k_r)$. The EWP is easily obtained from the SFA, taking only seconds. The electron–ion scattering cross sections depend only on k_r. They can be calculated using scattering theories and computer codes developed over the past few decades. The relative accuracy of these theoretical methods has been mostly well understood. To deal with the experimental uncertainty in the laser parameters used, one can adjust the laser intensities in the calculation to find best agreement with measurements.

QRS has another far-reaching consequence for strong-field rescattering physics. Since the role of lasers and electron–ion scattering phenomena are separable, one can extract field-free electron–ion scattering information from laser-generated spectra, and the results should be independent of the laser pulses used. These electron–ion scattering cross sections are not different from those obtained in conventional electron scattering experiments. They can be used to reveal the structure of the target. Thus, QRS provides a firm theoretical foundation for imaging the structure of the target. Since laser pulses of a few femtosecond durations are currently available, in principle, laboratory intense laser pulses can be developed into powerful tools for imaging time-dependent chemical or biochemical reactions.

QRS is a theoretical model which has been around for just about 2 years. In three extended publications we have applied the theory to HATI spectra [35], HHG spectra [36] and NSDI processes [37]. Examples from these published works will be used in this review only to illustrate how QRS is applied to these different problems. It is a theory that is still under development. As QRS is generalized to more complex systems, additional ingredients, especially those associated with dynamic systems, need to be added.

The QRS theory is built upon the rescattering model that was first developed in the 1990s. As shown in this review, rescattering phenomena encompass a wide range of strong-field physics. Clearly it is not possible to cite all the important works from the last two decades. Readers who wish to follow the developments of strong-field rescattering physics should consult various review papers from the past decade. This review is organized into different sections that can be read independently. After the initial introduction of QRS, readers
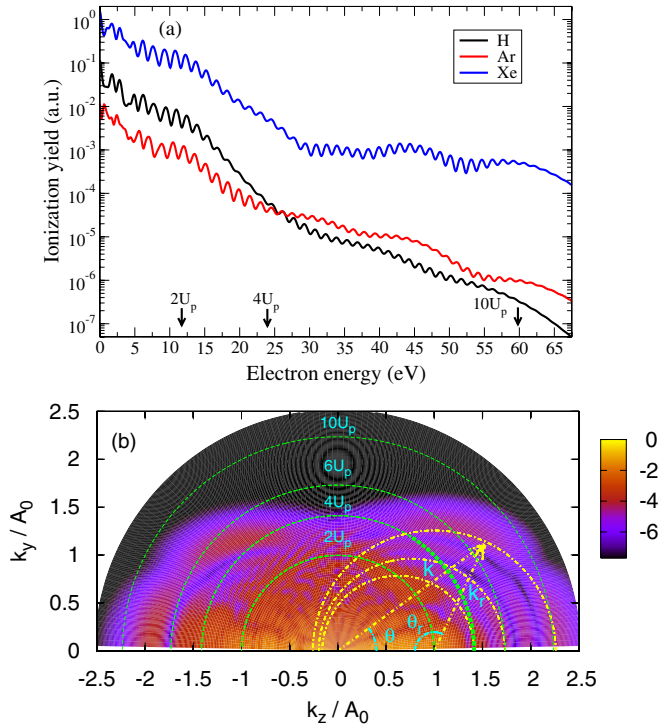
Figure 1. (a) Photoelectron energy distributions (in logarithmic scale) calculated for H, Ar and Xe by solving the TDSE. The laser is a 5 fs pulse, at the peak intensity of 1.0×10^{14} W cm^{-2} and wavelength of 800 nm. (b) 2D momentum distributions. Photoelectrons of a given energy are represented on a concentric circle centred at the origin. The elastic scattering of a returning electron with momentum k_r in the laser field is represented by a half-circle with its centre shifted from the origin by $A_r = k_r/1.26$. A_0 is the peak value of the vector potential.

should be able to jump to sections where a specific rescattering phenomenon is addressed.

2. Strong-field physics and quantitative rescattering theory for atomic targets

2.1. The need of a quantitative theory for ATI and HHG spectra

Strong-field physics deals with phenomena where the strength of the laser field is comparable to the electric field in an atom or molecule. In principle this creates a rather complex interplay on the electrons in the system. Fortunately many phenomena can be understood qualitatively based on simple pictures. In some cases, classical models can often capture the essence of the phenomena, but for quantitatively correct results quantum calculations are needed.

Consider exposing a hydrogen atom, an Ar and a Xe atom, to an 800 nm Ti-sapphire laser pulse with a peak intensity of 10^{14} W cm^{-2} and a pulse duration of 5 fs. Experimentalists can measure above-threshold ionization (ATI) photoelectron spectra [38] or HHG spectra [39]. Theoretically one can calculate ATI and HHG spectra by solving the TDSE [40–43] using the single active electron approximation, as has been done since the 1990s. Figure 1(a) shows the calculated ATI electron spectra for the three targets. In the figure, three

specific energies of 2, 4 and $10U_p$ are marked. For all three, the electron spectra display the characteristic fast exponential drop-off at low energies till about $2U_p$. Then the drop-off slows down between $4U_p$ and $10U_p$ before the fast drop-off picks up again beyond $10U_p$.

A qualitative understanding of these general features based on classical physics has been available since the early 1990s. Based on the tunnelling picture, electrons are released from the atom initially with near-zero velocity. They are then accelerated in the laser field and acquire a momentum given by the vector potential at the time of tunnelling ionization. These direct electrons can reach a maximum kinetic energy of $2U_p$. The plateau electrons (those electrons from about $4U_p$ to $10U_p$) are due to the backscattering of the returning electrons by the target ion. According to such a model, the $2U_p$ and $10U_p$ cutoffs depend only on the peak intensity of the laser field, not on the target.

A closer look at the spectra of figures 1(a) reveals that the HATI spectra are only approximately described by such a simple model. In particular, the $2U_p$ and $10U_p$ cutoffs are not clearly noticeable. For the plateau electrons, the plateau is much flatter in Xe than in Ar and H. Since the same laser pulse was used for the three targets, the difference in the spectra must be due to the nature of the target. In other words, HATI spectra indeed depend on the target, but in what ways? Can one incorporate the target structure into the rescattering model?

2.2. Theoretical tools for HATI and HHG

2.2.1. Atoms in a laser field—TDSE and SFA.
To obtain HATI photoelectron and HHG spectra, in principle one can perform the brute force numerical solution of the many-body TDSE. In reality, both HATI and HHG processes are initiated by returning electrons which form only a tiny fraction of the full electronic wavefunction; thus, it is very difficult to achieve good accuracy based on purely numerical methods. By limiting ourselves to one-electron model atoms in a short linearly polarized laser field, however, accurate numerical solutions of the TDSE can be achieved without too much effort using our own code [42], or similar codes developed by others. To model one-electron atoms, a spherically symmetric model potential $V(r)$ is adopted [41, 44]. The model potential is chosen such that it generates the energies of the ground state and of the first few excited states accurately. By treating these spectra as 'experimental results' where the property of the laser and the 'structure' of the atom are fully known, we examine whether one can establish a quantitative theory based on the rescattering concept. We comment that in real experiments, the laser beam is focused and electron spectra are collected from a volume of smoothly varying peak intensities [45]. Such experimental data are inconvenient for the purpose of establishing a new theoretical model.

In the past two decades, the interaction of lasers with atoms has also been treated approximately using the SFA. For clarity, we define the first-order SFA describing the direct electrons as SFA1:

$$f_1(\mathbf{k}) = -i \int_{-\infty}^{\infty} dt \langle \chi_{\mathbf{k}}(t) | H_i(t) | \Psi_0(t) \rangle. \tag{1}$$

Here Ψ_0 is the initial state, H_i is the laser–electron interaction and $\chi_\mathbf{k}$ is the Volkov state. To describe rescattering, a second-order SFA (SFA2) [29, 30, 32] is needed. For SFA2, the scattering amplitude can be written as

$$f_2(\mathbf{k}) = -\int_{-\infty}^{\infty} dt \int_{t}^{\infty} dt' \int d\mathbf{p} \langle \chi_\mathbf{k}(t') |V| \chi_\mathbf{p}(t') \rangle$$
$$\times \langle \chi_\mathbf{p}(t) |H_i(t)| \Psi_0(t) \rangle. \tag{2}$$

Here, the electron is first ionized at time t and rescattered at time t'. The potential V is the electron–ion interaction, i.e. the model potential chosen. Integration over the momentum is carried out using the saddle-point approximation.

A similar SFA2 equation can also be written down for the induced dipole moment by the laser field, for atoms in [27] and for molecules in [46–48]. A length gauge was used in our SFA2 model, but the velocity form has also been used in other applications. Details of these standard numerical methods can be found in [35, 36].

2.2.2. Elastic electron–ion collisions and photo-recombination processes.
Within the one-electron model, field-free elastic electron–ion collisions and photo-recombination processes can also be calculated 'exactly' by solving the time-independent Schrödinger equation. The former is the same as the typical potential scattering treated in all graduate quantum mechanics textbooks [49]. Since the model potential $V(r)$ for a neutral atom has the Coulomb form at large distance r, it is convenient to express $V(r) = V_S(r) - 1/r$, where $V_S(r)$ is a short-range potential. The elastic scattering amplitude is then expressed as

$$f(\theta) = f_c(\theta) + \hat{f}(\theta), \tag{3}$$

where f_c is the analytical Coulomb scattering amplitude, and the scattering amplitude $\hat{f}$ from the short-range potential is calculated using a partial wave expansion. The detailed expressions are given in [35]. Note that the modulus square of f_c gives the familiar Rutherford scattering cross section which decreases smoothly with increasing scattering angles and with increasing scattering energies. The $\hat{f}$ is from the short-range potential $V_S(r)$; thus, only a few partial waves are needed for convergence. This term, together with the interference with f_c, contributes to the oscillatory structure in the DCS. These structures are understood as the diffraction of electrons by the target ion. No oscillatory structure is present if the electron is approximated by a plane wave or by a Coulomb wave for atomic targets.

Calculation of photoionization cross sections has also been treated in standard textbooks. As an example, for Ar and Xe, the valence orbital has angular momentum $\ell = 1$; thus the continuum electron after photoionization has $\ell = 0$ and 2. For HHG, there are minor changes in the relevant dipole matrix elements. The initial state is a continuum electron incident along the direction of laser polarization. The specific dipole matrix element for Ar, for example, is given by Le *et al* [36]:

$$\langle \Psi_i |z| \Psi_k^+ \rangle = \frac{1}{\sqrt{3\pi k}} \big[e^{i(\sigma_0+\delta_0)} \langle R_{31}|r|R_{E0} \rangle /2$$
$$- e^{i(\sigma_2+\delta_2)} \langle R_{31}|r|R_{E2} \rangle \big]. \tag{4}$$

It depends on the radial wavefunction R_{31} for the 3p orbital, and $R_{E\ell}$ for the continuum electron, the Coulomb phase shift σ and the phase shifts due to the core potential δ, for partial waves $\ell = 0$ and 2. The radial integrals are real numbers but the phases make the dipole matrix element a complex number in general. If plane waves are used to represent the continuum electron, the phases are zero and the dipole matrix element becomes a real number or a pure imaginary number. Details of the calculations of dipole matrix elements can be found in [36].

2.3. Quantitative rescattering theory for HATI electrons

2.3.1. Characterization of the returning electron wave packet.
Using the TDSE one can obtain accurate momentum spectra of HATI electrons, $D(k, \theta)$, where k is the momentum of the photoelectron and θ is measured with respect to the polarization axis. According to the rescattering model, these high-energy photoelectrons are the result of elastic scattering of the returning electrons by the target ion. Let the kinetic momentum of the electron be k_r, and the angle of scattering with respect to the 'incident' (towards the target ion) direction be θ_r. From the given model potential, the DCS, $\sigma(k_r, \theta_r)$, can be calculated. Since the elastic collision occurs in the laser field, the photoelectron momentum along the direction of the laser polarization will gain an additional momentum as it exits from the laser field. Thus

$$k_z = k \cos\theta = -A_r \mp k_r \cos\theta_r,$$
$$k_y = k \sin\theta = k_r \sin\theta_r \tag{5}$$

(see figure 1(b)). Here z is the direction parallel to the polarization axis of the laser, and y is perpendicular to it. For atomic targets, the electron momentum spectra have cylindrical symmetry. Along the polarization axis, the additional momentum gain is $-A(t_r) = -A_r$, where t_r is the instant of electron recollision. For electrons returning with the maximum kinetic energy of $3.2U_p$, at the time of recollision, the vector potential is maximum, i.e. A_0. The relation between k_r and $A(t_r)$ is given by $k_r = 1.26A_0$. For electrons returning with less kinetic energy, according to the classical model, each may take two distinct paths, corresponding to the long and the short trajectories, respectively. But at the time of return, they have an identical value of A_r. For simplicity, we set the relation between k_r and A_r by $k_r = 1.26A_r$. Note that the approximation $k_r = 1.26A_r$ implies that the model works better for energies closer to the high-energy part of the plateau region. We assess the degree of accuracy of this approximation by comparing the QRS with accurate numerical results from TDSE.

Figure 1(b) shows a typical 2D electron momentum spectra calculated from solving the TDSE. From the two equations in (5), there is a one-to-one relation between (k, θ) and (k_r, θ_r). Equations (5) can be solved for θ and k in terms of θ_r and k_r,

$$\tan\theta = \frac{\sin\theta_r}{\pm(1/1.26 - \cos\theta_r)}, \tag{6}$$

$$k^2 = k_r^2(1.63 - 1.59\cos\theta_r), \tag{7}$$
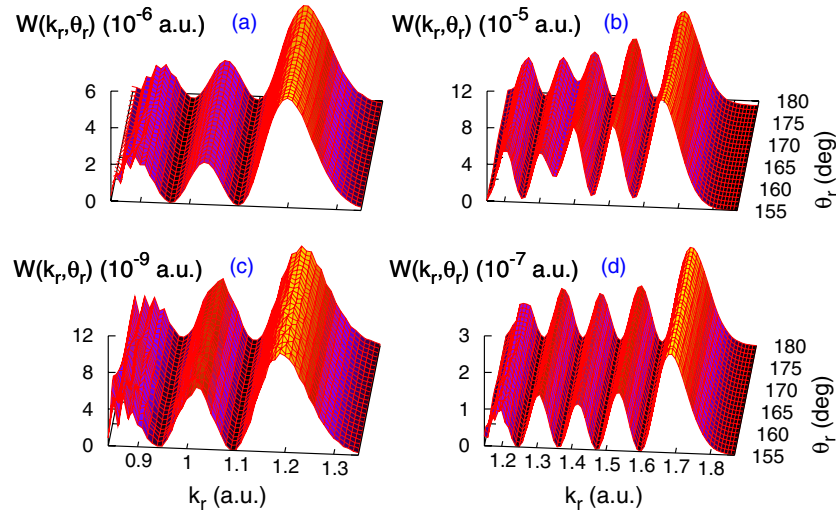
Figure 2. Right-side wave packets extracted from the electron momentum distributions calculated using the TDSE and SFA2, for single ionization of Ar in a 5 fs laser pulse with the wavelength of 800 nm. Left column: from the TDSE (top) and SFA2 (bottom), at an intensity of 1.0×10^{14} W cm^{-2}; right column: same, but at 2.0×10^{14} W cm^{-2}.

where the + and − sign refers to electrons scattered to the + side or the − side of the z-axis, respectively.

Following the rescattering picture, we define a ratio

$$W(k_r, \theta_r) = D(k, \theta)/\sigma(k_r, \theta_r). \tag{8}$$

In figure 2 we show the $W(k_r, \theta_r)$ for two sets of laser pulses with different peak intensities. Note that the range of k_r is limited to the region close to the cutoff, and the θ_r is limited to large angles to ensure that there is no contribution from direct ionization by the laser. Along the upper row they were obtained using the 'exact' TDSE and DCS, while along the lower row they were obtained from SFA2, with the DCS calculated using the first-Born (B1) approximation, respectively. Recall that in SFA2 and B1, the continuum electron wavefunction is approximated by a plane wave. Figure 2 shows two important features. First, for a given k_r, $W(k_r, \theta_r)$ is nearly independent of θ_r. This allows us to rewrite $W(k_r, \theta_r) = W(k_r)$. For simplicity, we call $W(k_r)$ the returning electron wave packet. Similarly, a wave packet $W_{SFA}(k_r)$ can also be obtained from the SFA2 model. Second, the $W(k_r)$ obtained from SFA2 has the same k_r dependence as the one from solving the TDSE. Put these two features together, we suggest that one can use $W_{SFA}(k_r)$ for $W(k_r)$, thus bypassing the need to solve the TDSE. We thus proposed the QRS theory for the HATI spectra where $D(k, \theta)$ is obtained from

$$D(k, \theta) = W(k_r)\sigma(k_r, \theta_r), \tag{9}$$

where $W(k_r)$ is the $W_{SFA}(k_r)$ calculated from SFA2. This equation has the form of the standard scattering theory. For each k_r, the 'incident' electron is scattered into an angle θ_r. This is precisely the last step of a typical rescattering process, but now there is a mathematical expression describing how the calculations can be carried out, as shown in equation (9). As the scattered electron leaves the laser field, it gains an additional momentum $-A_r$ along the polarization direction,

as depicted in equations (5). Note that $W(k_r)$ in fact should be understood as the incident returning electron flux integrated over the laser pulse duration. It is called a wave packet for simplicity in connection with the classical rescattering picture. $W(k_r)$ includes the wave packet interference from rescattering at different times.

The concept of a wave packet that can be calculated is the essential ingredient of the QRS theory. We thus examine it further. In figures 3(a) and (b) we compare the wave packets at three scattering angles, for $\theta_r = 160°$, $170°$ and $180°$, obtained from solving the TDSE for Ar, for a five-cycle and an eight-cycle pulse, respectively. The electric field and vector potential of each pulse are shown in figures 3(c) and (d), respectively. The wave packets, more precisely the envelopes, are clearly independent of the angles θ_r, thus confirming the general validity of $W(k_r, \theta_r) = W(k_r)$. In figures 3(e)–(h), we compare the left- and right-side wave packets for three targets, H, Ar and Xe, for an eight-cycle pulse, obtained from the TDSE and from SFA2. From such a comparison, one can generally expect that the wave packets obtained from SFA2 will introduce a shift of about 2–3% for different targets. The errors are due to the neglect of electron–target ion interaction during the propagation of the wave packet. Forgoing these differences, to the first order, the wave packet can be regarded as being independent of the target.

The fact that the wave packets, $W(k_r)$, derived from SFA2 and from the TDSE are nearly identical may at first appear to be surprising. However, with hindsight this is not difficult to understand. The electron first tunnels out at the outer edge of the atom. Then it drifts out under the electric field of the laser. During this propagation process, the electron spends most of the time away from the target ion. Thus, its motion is controlled to a large extent by the laser field, but not much by the potential from the ion core. Since SFA2 includes the dominant electron–laser field interaction exactly, the wave packet derived from SFA2 is quite close to the one from the TDSE.

To see how the DCS for different targets differ from each other, in figure 4 we compare the DCS for electron collisions
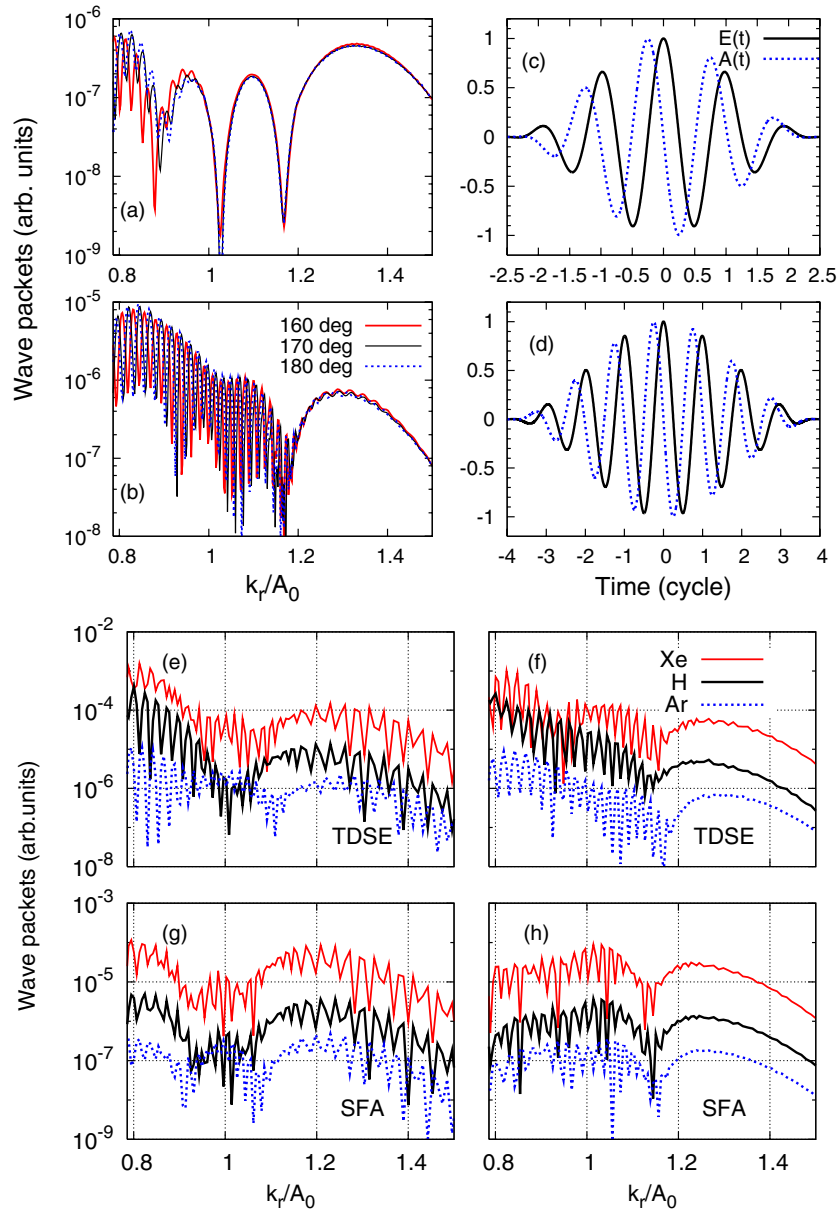
Figure 3. (a) Right-side wave packets ($k_z > 0$) extracted from the TDSE for single ionization of Ar in a five-cycle pulse with the wavelength of 800 nm at the intensity of 1.0×10^{14} W cm^{-2} at $\theta_r = 160°$, $170°$ and $180°$, respectively; (b) same as (a) but for an eight-cycle pulse; (c), (d) electric field and vector potential used in (a), (b), respectively. The peak values of both $E(t)$ and $A(t)$ are normalized to 1. (e) Left-side wave packets ($k_z < 0$) extracted from the TDSE for single ionization of H, Ar and Xe in an eight-cycle pulse at the peak intensity of 1.0×10^{14} W cm^{-2} with the wavelength of 800 nm, respectively; (f) same as (e) but for the right-side ($k_z > 0$); (g) same as (e) but from SFA2; (h) same as (f) but from SFA2.

with Ar$^+$, Kr$^+$ and Xe$^+$ ions with electron momentum from 0.8 to 1.2 au. We note that the DCS of Xe exhibits much more pronounced diffraction peaks in this energy region than the other two atoms. In particular, the DCS for Xe at larger k_r has a large peak near the scattering angle of $180°$. This behaviour, after integrated over the scattering angles, explains why the HATI electron energy spectra of Xe is much flatter than in the case of Ar, as shown in figure 1(a). For more examples, see [34, 50].

2.3.2. Extracting the DCS from HATI spectra. An important consequence of the QRS model, according to equation (9),

is that one can extract the DCS, $\sigma(k_r, \theta_r)$, for a fixed k_r, from the HATI momentum spectra, and the results should be independent of the laser used—that is, independent of laser's intensity, pulse duration and wavelength. How accurate is this model? In figure 5, we illustrate the DCS extracted from the HATI spectra calculated by solving the TDSE for two laser intensities. The extracted DCS from the HATI spectra indeed agree well with each other and with the DCS directly calculated from electron–Ar$^+$ collisions. We comment that in QRS, the absolute yield is not given. Thus, the extracted DCS must be normalized. In this example, we noticed that the DCS extracted from the higher laser intensity spectra has a larger discrepancy. This is due to the approximation
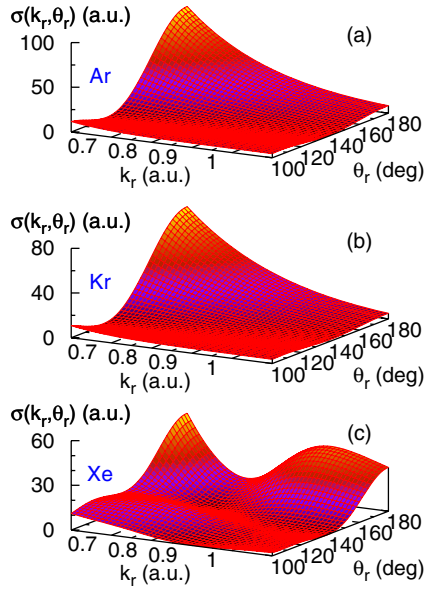
Figure 4. Two-dimensional 'exact' elastic differential scattering cross sections for (a) Ar, (b) Kr and (c) Xe, respectively.
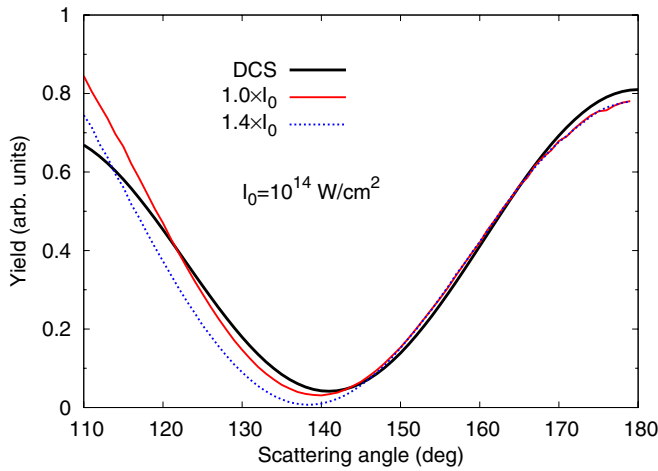
Figure 5. Elastic scattering DCSs for Ar at fixed $k_r = 1.22$ (thick black solid line) compared with the DCS extracted from the 2D HATI electron momentum distributions calculated from solving TDSE for a five-cycle laser pulse with the wavelength of 800 nm at intensities of 1.0 (thin red solid line) and 1.4×10^{14} W cm^{-2} (dotted line), respectively.

$k_r = 1.26 A_r$ used in QRS which was established only for $A_r = A_0$.

2.3.3. Comparison with experimental HATI spectra. Up to this point, the HATI spectra were obtained from a laser pulse with fixed peak intensity. Experimentally the intensity distribution of a focused laser beam is not uniform in space. The HATI electrons are collected from the focal volume. Thus, to compare with experimental data, theoretical calculations must include the volume effect. For a laser pulse with peak intensity I_0 at the focal point, the total photoelectron yield is

written as

$$S(\mathbf{k}, I_0) = \rho \int_0^{I_0} D_I(k, \theta) \left(\frac{\partial V}{\partial I} \right) dI, \qquad (10)$$

where ρ is the density of the atoms, and dV/dI is the isointensity shell. Its explicit expression is given in [35] if the spatial distribution is Lorentzian in the propagation direction and Gaussian in the transverse direction. If $D_I(k, \theta)$ is calculated using QRS, then the DCS, which does not depend on the laser peak intensity, can be factored out of the integral, and equation (10) becomes

$$S(\mathbf{k}, I_0) = \bar{W}_{I_0}(k_r)\sigma(k_r, \theta_r), \qquad (11)$$

where we have defined a volume-integrated wave packet for the whole focused laser pulse. Equation (11) implies that one can express the experimental HATI spectra in the form of a volume-integrated wave packet $\bar{W}$ multiplied by the DCS. As shown below, equation (11) makes it possible to extract the DCS directly from experimental HATI spectra. Since the wave packet at a given k_r enters as an overall multiplicative factor, the DCS can be obtained from experimental HATI spectra without knowing the nature of the laser pulse used.

*2.4. Separability of lasers and targets in the HATI spectra*

The significance of equations (9) and (11) should not be overlooked by their simplicity. They have far-reaching consequences. Its validity is essential for retrieving the structure of the target from the HATI momentum spectra. Structure retrieval is an inverse scattering problem and if the scattering theory is not correct and simple, the structure information cannot be conveniently retrieved.

*2.4.1. Extracting the DCS from experimental HATI spectra.* Equation (11) shows that, for a fixed k_r, the relative DCS can be directly obtained from the momentum spectra of the HATI electrons. Recall that (k, θ) and (k_r, θ_r) are related by equations (6). Thus to obtain the relative DCS, see figure 1(b), one just has to read off the HATI yields along $k_r = $ constant. According to QRS, the normalized DCS thus obtained should be independent of the lasers used. Figure 6 shows an example where the DCS were extracted from the experimental HATI spectra [51] for Xe$^+$ and for Ar$^+$. For each target, four sets of DCS were extracted from four HATI spectra using lasers of different carrier-envelope phases (CEPs) (see section 2.5 below). It is clear that the four sets of DCS extracted from the experiments are quite close to each other. When compared to the DCS calculated theoretically, the agreement is quite good. The theoretical DCS has a sharper minimum since the angular resolution of the experiment has not been included. Additional examples can be found in [52, 53].

2.4.2. Species dependence and laser wavelength dependence of HATI spectra. Using QRS, the wave packet only depends on the laser's properties. Thus, the target dependence of the HATI spectra is entirely due to the DCS of the target in the energy region of the returning wave packet. In figure 7(a),
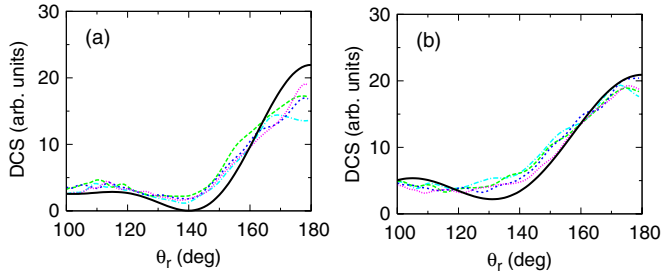
Figure 6. (a) Differential elastic scattering cross sections for Xe^+ ions by free electrons with incident momentum of $k_r = 1.2$ au. Solid line: theoretical result calculated from a model potential for Xe. Dashed lines: DCS extracted from experimental data of [51] with different CEPs. (b) Similar to (a) except for Ar, for $k_r = 0.9$ au.
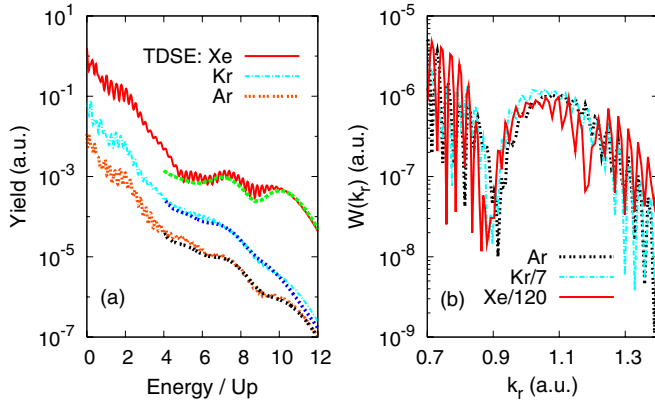
Figure 7. Single ionization of Xe, Kr and Ar atoms by a five-cycle laser pulse with a wavelength of 800 nm and peak intensity of $I_0 = 1.0 \times 10^{14}$ W cm^{-2} ($A_0 = 0.94$). (a) Comparison of the angle-integrated electron energy spectra from the TDSE (long lines from 0 to $12U_p$) and from the QRS model (short lines above $4U_p$). The QRS energy spectra for Kr and Xe are calculated using the wave packet extracted from Ar, with proper normalization at one energy point. (b) Normalized momentum distributions of the returning electron wave packets extracted from the 'left-side' ($k_z < 0$) of the momentum spectra.

the total electron energy spectra for Xe, Ar and Kr calculated from solving the TDSE are shown. The laser used has a wavelength of 800 nm and a peak intensity of 1.0×10^{14} W cm^{-2}. Figure 7(b) shows that the wave packets from the three targets are quite similar after being renormalized. Using the wave packet from Ar and QRS to calculate the electron spectra for all three targets, we obtained the total electron energy spectra. The results are shown in figure 7(a) for each atom after the spectra are normalized at a single electron energy. They are shown to be in good agreement with those from solving the TDSE. These results illustrate that the HATI spectra are entirely determined by the DCS if different targets are exposed to identical laser pulses.

One can also use the QRS model to explain the experimental wavelength dependence of the HATI spectra for a fixed peak intensity. In [54], HATI spectra for a peak intensity of 0.8×10^{14} W cm^{-2}, for lasers with a wavelength of 800, 1300, 2000 and 3600 nm, respectively, have been reported. To compare with experimental results, as shown in [35], SFA2 calculations were carried out and

volume-integrated wave packets were obtained. Since the returning electron momentum is proportional to the wavelength, longer wavelength lasers generate electrons with higher momenta. The volume-integrated wave packets, for the long pulses used in the experiment, are quite flat till near the cutoff at $3.2U_p$. In figure 8, the DCS of Ar, $\sigma(k_r, \theta_r)$, for the respective returning energy region are shown. It is interesting to note that the DCS for k_r between 1.9 and 2.5 au, the typical momentum range for the 2000 nm laser at this intensity behave very similar to the DCSs for Xe with k_r in the region between 0.8 and 1.2 au for an 800 nm laser at an intensity of about 1.0×10^{14} W cm^{-2} (see figure 4(c)), namely the DCS is quite large at large angles close to $180°$. Thus for 2000 nm, the electron energy spectra is expected to be quite flat, similar to the Xe curve in figure 7(a). In figure 9, the total electron spectra calculated from QRS are compared to the experimental data of [54]. Very good agreement can be observed and the 2000 nm data indeed show a very flat plateau.

From these examples, one can conclude that the HATI momentum spectra or photoelectron energy spectra in the rescattering energy region of 4–$10U_p$ are solely determined by the DCS of the field-free electron–target ion collisions. More examples can be found in [50].

### 2.5. Carrier envelope phase and retrieval of laser parameters of few-cycle pulses

2.5.1. Left/right asymmetry of HATI electrons by few-cycle laser pulses. According to the rescattering model, the returning electrons will visit the target ion from the left or the right side of the polarization axis in each half-cycle. For long pulses the HATI spectra on the two sides are identical. This is not the case for few-cycle pulses. For these pulses, the electric field can be written in general in the form of $E(t) = E_0(t) \cos(\omega t + \phi)$, where $E_0(t)$ is the amplitude, ϕ is the CEP and ω is the central angular frequency. Recent advance in laser technology has made it possible to 'stabilize' the CEP of a few-cycle pulse, and a number of experiments have shown left/right asymmetry along the polarization axis of the emission of photoelectrons [55–57], of the ion momentum distributions in nonsequential double ionization of atoms [58], as well as asymmetry in the dissociative ionization of molecules [59–63]. CEP-stabilized laser pulses are also essential for the generation of attosecond pulses [64–66]. While experimentally the relative CEP can be controlled, the determination of the absolute value of the CEP relies on theoretical simulations [55, 58, 67–69].

Several techniques have been proposed to determine the absolute CEP of few-cycle pulses, but most of them are based on analysing the left/right asymmetry of the HATI spectra. To retrieve the CEP by comparing theoretical calculations with experimental HATI spectra, theoretical calculations must be carried out over many intensities to include all the electrons from the focal volume. Since the asymmetry also depends on pulse duration and peak intensity of the laser, and they are not known accurately, this makes the determination of CEP even more complicated. To generate HATI spectra by solving the TDSE needed for the CEP determination is thus not practical due to the large number of calculations to be performed.
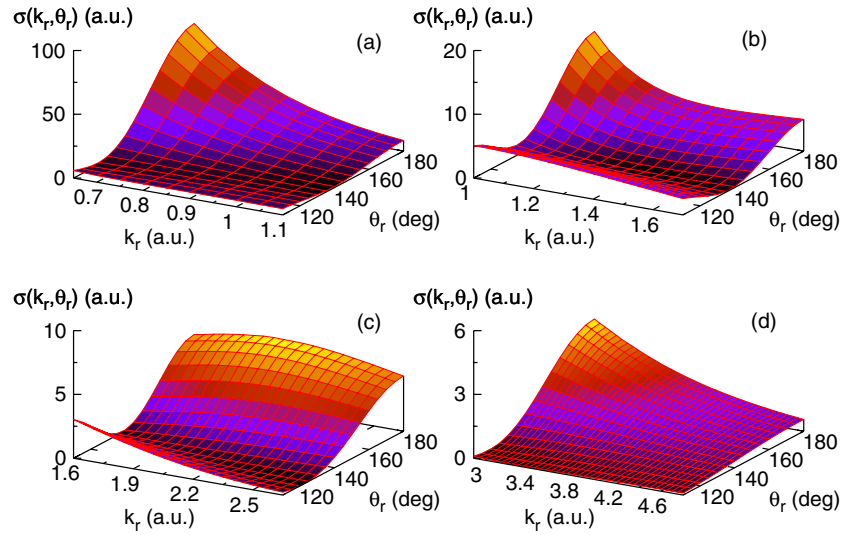
Figure 8. DCSs for elastic scattering of electron with Ar$^+$ at large scattering angles of $110°$–$180°$. The incident electron momenta are (a) 0.65–1.10, (b) 1.00–1.75, (c) 1.60–2.65 and (d) 2.95–4.80, corresponding to the high-energy plateau regions for lasers of wavelength of 800 nm, 1300 nm, 2000 nm and 3600 nm, respectively.
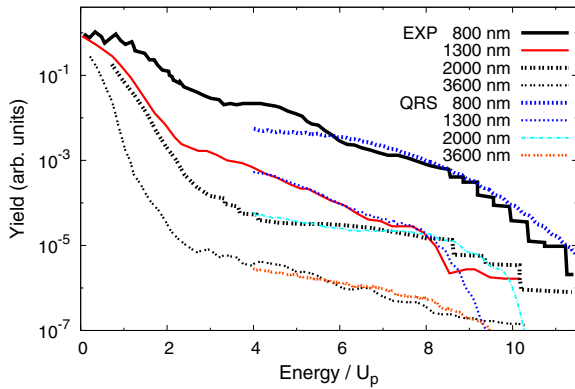

Figure 9. Comparison of experimental and QRS angle-integrated photoelectron energy spectra for single ionization of Ar by few-cycle laser pulses at the peak intensity of 0.8×10^{14} W cm^{-2} with wavelengths of 800 nm, 1300 nm, 2000 nm and 3600 nm, respectively. The experimental measurements are taken from [54]. The QRS results starting from $4U_p$ are normalized to the experimental data individually at high energies to get the best fit. Electron energies are expressed in units of U_p.

According to QRS, all the properties of the laser pulses in the HATI spectra are 'contained' in the wave packet $W(k_r)$, or more precisely, in the volume-integrated wave packet, $\bar{W}(k_r)$. If HATI spectra were measured from atomic targets such as Xe, where the DCS are well known, then from the experimental HATI spectra, the volume-integrated wave packet on the left, $W_L(k_r)$, and the one on the right, $W_R(k_r)$, from each measurement can be obtained. Using QRS, for each peak intensity I_0 at the laser focus, pulse duration τ and CEP, the left and right wave packets can be readily calculated. Since the wave packets in QRS are obtained from SFA2, such calculations are many thousands of times faster than from solving the TDSE. Thus QRS provides a much more efficient method for the retrieval of laser parameters.

2.5.2. CEP retrieval using left/right HATI electron momentum spectra.

Consider a five-cycle laser pulse at a peak intensity of 1.0×10^{14} W cm^{-2} and central wavelength of 800 nm, with a CEP of 0 and $\pi/2$, respectively. Their electric fields and vector potentials are shown in figures 10(a) and (c) and their electron wave packets extracted from SFA2 are shown in figures 10(b) and (d), respectively. In figures 10(a) and (c), the peaks of the electric field on the left (right) are labelled by an L (R) and the peaks of the vector potential on the left (right) are marked by an A (B). These symbols are also used in figures 10(b) and (d). Recall that the vector potential determines the momentum of the returning electron and the electric field determines the tunnelling ionization rate. From the captions in these figures, one can clearly see how the peak positions of the left/right wave packets shift as the CEP is varied. By focusing on the outer portion of each wave packet, in figures 11(a) and (b) we observe the smooth variation of the left and right wave packets as the CEP is varied. Using QRS, as shown in figures 11(c) and (d), we predict that the electron spectra (after integrating over a cone of $10°$ along the polarization axis) also shift progressively with the increase of the CEP.

To compare with experimental data, the theoretical electron spectra must be integrated over the focal volume. The electron spectra are then compared to experimental data. To achieve best overall agreement, the peak intensity and pulse duration in the theoretical calculations have to be varied as well. In the method used in [69], the peak positions of the electron spectra are identified visually by comparing with data from [51]. The method also relies on the assumption that the relative CEP in each successive step in the measurement is fixed. In [69], a peak intensity of 1.1×10^{14} W cm^{-2} and pulse duration of 6.7 fs were retrieved. These parameters differ somewhat from the values of 1.0×10^{14} W cm^{-2} and 6.0 fs claimed in [51].

2.5.3. CEP and laser parameter retrieval for single-shot laser pulses.

The CEP retrieval method described in section 2.5.2
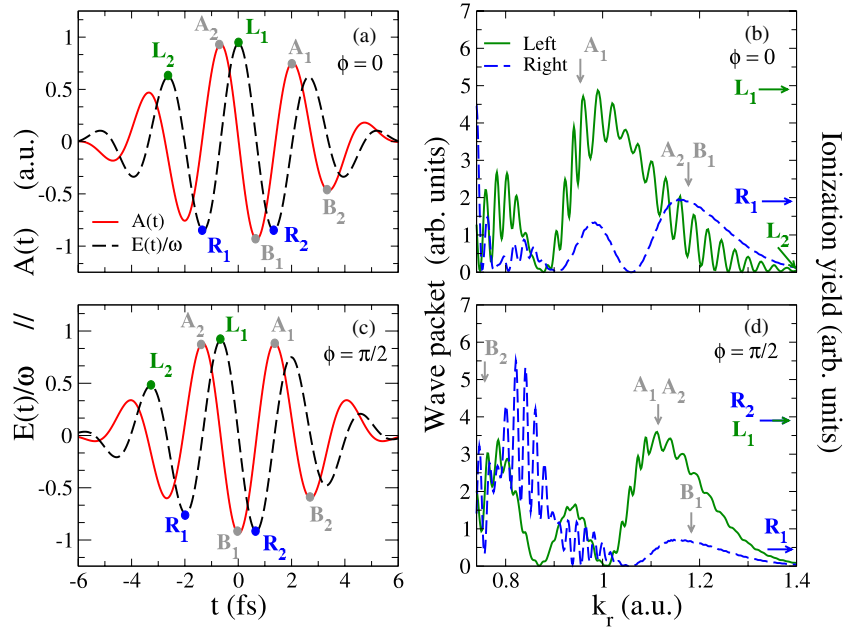
Figure 10. Temporal evolutions of electric fields and vector potentials for five-cycle laser pulses at the peak intensity of 1.0×10^{14} W cm^{-2}, with the wavelength of 800 nm and carrier-envelope phases of $\phi = 0$ (a) and $\phi = \pi/2$ (c). Electron wave packets extracted from SFA2 for the left and right sides for $\phi = 0$ (b) and $\phi = \pi/2$ (d). In (b), (d) the vertical arrows indicate the expected peak electron momenta when the electrons return at the corresponding peak vector potentials shown by identical labels in (a), (c). The horizontal arrows indicate the relative tunnel ionization rates when electrons are ionized near the peak electric fields shown by identical labels in (a), (c).
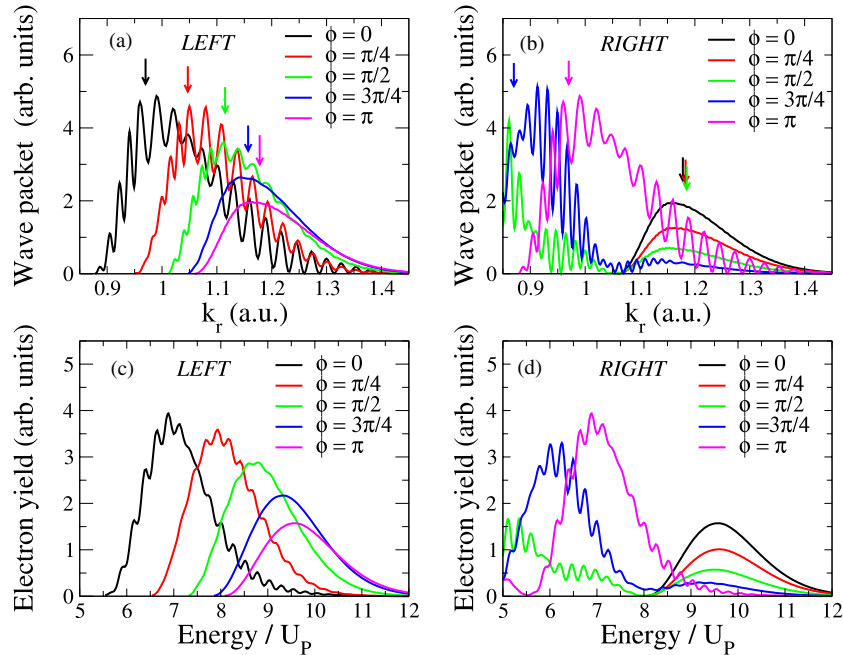

Figure 11. Electron wave packets extracted from the left (a) and right (b) sides for a laser pulse with a peak intensity of 1.0×10^{14} W cm^{-2}, pulse duration of five cycles, mean wavelength of 800 nm and different carrier-envelope phases. The arrows indicate the expected peak momenta from the peak vector potentials of the half-cycles responsible for the wave packet for the different absolute phases. (c), (d) Corresponding high-energy photoelectron spectra determined by means of the QRS model for xenon atoms. The spectra are calculated by integrating over a cone of 10° along the laser polarization axis.

works, but the method is limited and still rather tedious. First, it relies on locating the peak or the cutoff position of the HATI spectra on the left and on the right visually. Second, only one energy point was used from the whole spectrum on each side. It is preferable to use the whole electron spectra for

the CEP retrieval and to automate the method. The need to automate the retrieval method becomes even more urgent since Wittmann *et al* [70] have demonstrated that it is possible to obtain shot-to-shot HATI electron spectra. In typical few-cycle pulses, if the CEP was not stabilized, then each shot will have a
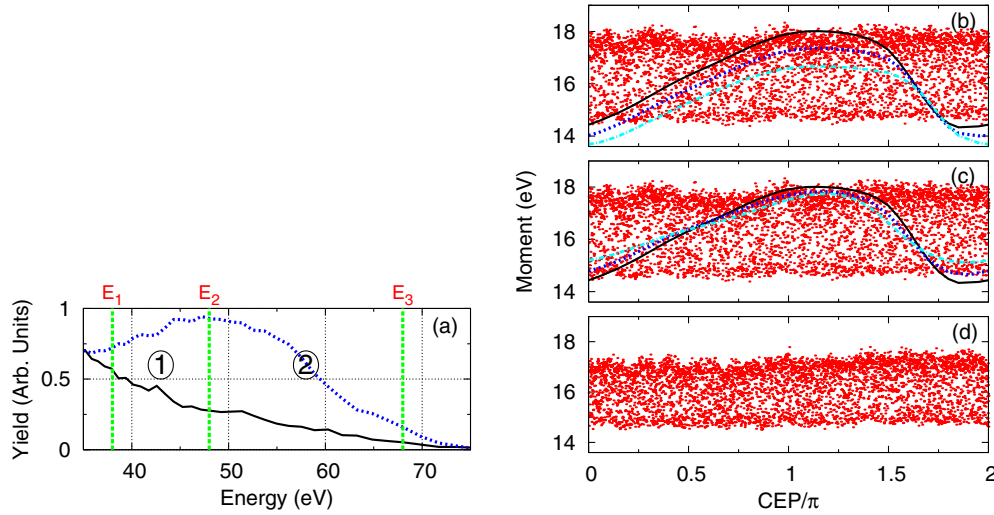
Figure 12. (a) Typical single-shot left- (solid line) and right-side (dashed line) electron energy spectra along the polarization axis. (b) Energy moment of left-side spectra from experimental measurements (dots) compared with theoretical calculations at peak intensities of 1.2 (dash-dotted line), 1.3 (broken line) and 1.4×10^{14} W cm^{-2} (solid line) with a pulse duration of 4.5 fs; (c) same as (b) but for theoretical calculations at the peak intensity of 1.4×10^{14} W cm^{-2} and pulse durations of 5.0 (dash-dotted line), 4.7 (broken line) and 4.5 fs (solid line), respectively; (d) energy moment of right-side spectra from experimental measurements. The experimental data are from [70].

different CEP. Thus the CEP of each shot must be determined independently. In [70], 4500 shots were recorded. Clearly the CEP for each of these shots has to be determined using a well-tested algorithm. This was achieved recently in [68] based on the QRS model. The method is robust and the laser pulses can be characterized in real time. By CEP-tagging each single laser shot, this opens up the opportunity of studying waveform-dependent processes with non-phase-stabilized pulses at any laser intensities and wavelengths.

The method used in [68] is to divide the HATI spectra along the polarization axis (or integrated over a small angular region about the axis) over a certain energy region. Figure 12(a) illustrates the left and right electron spectra of a typical single-shot measurement using Xe as the target. The spectral region chosen typically is for energies above about $5U_p$, and three energy points E_1, E_2 and E_3 are selected. From such energy spectra, a left and a right wave packet can be obtained. One then defines an energy moment M for each wave packet (left or right):

$$M = \frac{\int_{k_{r1}}^{k_{r3}} \left(k_r^2/2 \right) W(k_r) \, \mathrm{d}k_r}{\int_{k_{r1}}^{k_{r3}} W(k_r) \, \mathrm{d}k_r}. \tag{12}$$

Using the 4500 shots from [70], 4500 values of M's from the left-side wave packets are obtained. These calculated values are displayed in figure 12(b) where the horizontal axes are divided into 90 bins and each bin takes the values of M's per 50 shots. This is simply a way to distribute the M's and the value on the horizontal axis has no meaning. From figure 12(b), the mean values of M, or $\bar{M}'$, from the 4500 shots were calculated to be 16.46 eV. In figure 12(b), three curves of M values obtained from QRS for three intensities of 1.2, 1.3 and 1.4×10^{14} W cm^{-2} are shown. The average $\bar{M}$ for the three intensities are found to be 15.64, 16.05 and 16.46 eV, respectively. We have checked that the averaged $\bar{M}$ does not

depend on the pulse duration used. By comparing with the values extracted from the experimental data, we determined that the peak intensity used in the experiment was 1.4×10^{14} W cm^{-2}. In figure 12(c), three curves of M for lasers with the peak intensity of 1.4×10^{14} W cm^{-2} and pulse durations of 4.5, 4.7 and 5.0 fs are shown, respectively. The best fit to the experimental vertical width is used to obtain the pulse duration of 4.6 fs. Note that all 4500 shots were analysed but only the left wave packets were used. In principle, exactly the same information should be obtained from the right-side wave packets if the left and right detectors are identical. This is not the case since similar M's obtained from the right detector, as shown in figure 12(d), have lower moment values and the vertical width is smaller. Using the data from figure 12(d) a peak intensity of 1.33×10^{14} W cm^{-2} and pulse duration of 4.8 fs are obtained. These results are independent of the E_1 and E_3, or k_{r1} and k_{r3}, used in equation (12).

After the peak intensity and pulse duration are determined, the CEP of each shot can be obtained following the method used in [70]. By choosing an intermediate energy E_2, the total electron yields Y_L (Y_R) between E_1 and E_2 registered on the left (right) detectors are calculated. Define the asymmetry by $A_1 = (Y_L - Y_R)/(Y_L + Y_R)$. A similar A_2 is defined for electron yields between E_2 and E_3. By plotting the values (A_1, A_2) parametrically, Wittmann *et al* found these points form a ring with the shape of a 'potato', as shown in figure 13. Comparing with theoretical parametric plots calculated using a peak intensity of 1.4×10^{14} W cm^{-2}, and pulse durations of 4.5, 4.7 and 5.0 fs, respectively, it was found that a pulse duration of 4.6 fs gives the best overall fit. Note that the theoretical parametric plot is an ellipse. The experimental 'potato' shape is due to the different detector efficiency on the left and on the right. Based on such a comparison, the CEP for each laser shot can be read directly off from figure 13, by drawing a line from the centre of the ellipse to the experimental point. The

J. Phys. B: At. Mol. Opt. Phys. **43** (2010) 122001

Topical Review
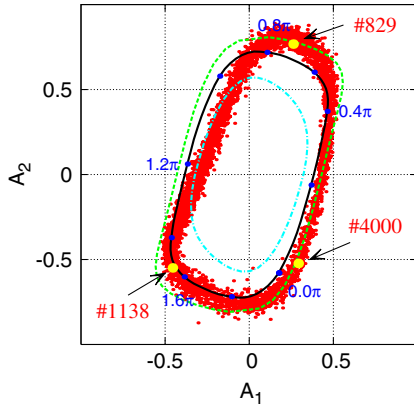
Figure 13. Comparison of the asymmetry ellipse from experiment with theory. The experimental points are calculated from the data of [70]. The peak intensity used in the theoretical simulations is 1.4×10^{14} W cm^{-2}. The energy range used is $(E_1, E_2, E_3) = (37.9, 57.5, 64.8)$ eV, and pulse durations used in theoretical simulations are 4.5 (broken line), 4.7 (solid line) and 5.0 fs (dash-dotted line), respectively. The CEP of each of the three shots from [70] can be read from such a parametric plot directly.

CEP of each laser shot is then obtained from the theoretical CEP value at the intersection of this line with the ellipse.

Thanks to QRS, the retrieval of laser parameters is very fast and the method can be programmed. By tagging the CEP of each single shot, CEP-dependent measurements can be carried out without phase stabilization, thus opening up opportunities of performing CEP-dependent measurements for lasers that still cannot be stabilized. The new method of phase retrieval used in [68] also reveals that the phase of the present-day 'phase-stabilized' laser pulse is 'stable' only up to 25° or so. Using single-shot data, Chen *et al* [68] were able to determine the CEP accurate to within 4 or 5°, based on the results obtained by changing values of E_1, E_2 and E_3 in the analysis. The method also provides a way to determine the peak laser intensity, pulse duration and CEP at the point where the laser interacts with the gas.

2.6. Nonsequential double ionization

Nonsequential double ionization (NSDI) is one of the most interesting rescattering phenomena in strong-field interactions of lasers with many-electron atoms and molecules. In NSDI, there are two mechanisms for the removal of the second electron by the returning electron. One is through electron-impact ionization, i.e. the (e, 2e) process, and the other is electron-impact excitation followed by laser tunnelling ionization. So far, QRS has been applied to study total NSDI yields of Ar versus laser intensity by Micheau *et al* [37], and more recently, the momentum correlation between the two outgoing electrons by Chen *et al* [71]. This topic has received a great deal of theoretical and experimental interest in the past years. References to earlier works can be found in [71] and [37].

2.6.1. Total double-ionization yields. To use QRS for calculating the total NSDI yield for a given laser peak intensity,
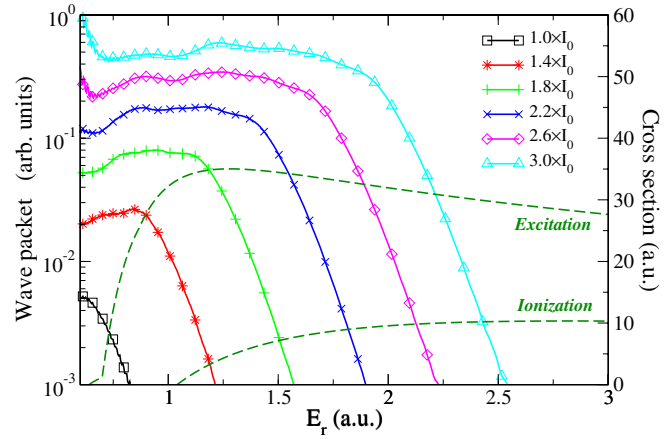

Figure 14. Volume-integrated electron wave packets extracted from photoelectron spectra on the 'right' side, for atomic argon singly ionized by a five-cycle laser pulse with a mean wavelength of 800 nm, for CEP equal to zero, and different peak intensities (with $I_0 = 1.0 \times 10^{14}$ W cm^{-2}). The total electron-impact ionization and excitation cross sections from the ground state of Ar$^+$ are also presented.

one first obtains the returning electron wave packet $W(E)$, either from theory or from the experimental HATI momentum spectra. One also needs electron-impact ionization cross sections and electron-impact excitation cross sections for each returning electron energy. For impact ionization, the semi-empirical expression of Lotz [72] is often used. For the Ar target the Lotz formula has been shown to be in good agreement with experimental measurements. For excitation cross sections, some empirical expressions must be derived. The details are given in [37].

According to the QRS model, the total NSDI yield is calculated from

$$\sigma^{++} = \int dE_r [W_L(E_r) + W_R(E_r)] \sigma(E_r), \qquad (13)$$

where $W_L(E_r)$ and $W_R(E_r)$ are the volume-integrated wave packets extracted from the left and right sides of the HATI spectra, and $\sigma(E_r)$ is the sum of electron-impact excitation cross sections and total electron-impact ionization cross section for incident energy E_r. The lower limits of the integrations are the excitation thresholds of each excited state or the ionization threshold. For Ar$^+$, if another electron is excited, say from 3p to 3d and all other higher excited states, the excited electron will be ionized subsequently by the laser. Thus all of these excited states contribute to the NSDI signal. In figure 14, total excitation cross sections and ionization cross section versus E_r, as well as the volume-integrated wave packets at different intensities, are shown. At low intensity, 1.0×10^{14} W cm^{-2} ($= I_0$), there is no NSDI since the cutoff energy of the wave packet is barely above the lowest excitation threshold. At 1.4 I_0, NSDI would originate almost entirely from the excitation processes. At even higher intensities, the contribution from impact ionization increases. However, since impact excitation cross sections for Ar$^+$ are much larger than impact ionization, contributions to NSDI come mostly from the excitation processes. In figure 15, the calculated
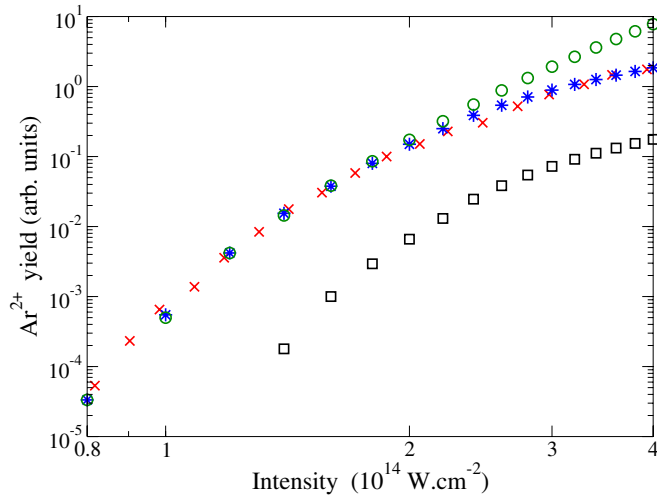
Figure 15. Non-sequential double ionization yield for argon atoms as a function of the peak intensity for a linearly polarized laser pulse with the mean wavelength of 800 nm. The red crosses are experimental results from [73] for a 30 fs pulse duration. The blue stars are from calculations when depletion effects and collisional ionization and excitation processes are considered. The results when depletion effects are omitted are shown as green circles, and the contribution when only direct ionization is included is represented by black squares.

NSDI yields versus the peak laser intensity are shown. The experimental data [73] and the calculations from QRS agree quite well when they are normalized to each other at one intensity. In the figure, we also see that impact ionization accounts only about 10% of the total NSDI yield. The figure demonstrates that at high intensities, one needs to account for the depletion effect where single ionization probability has reached 100%. This example illustrates that QRS can be used to explain NSDI yields by combining the returning wave packets with electron-impact ionization and electron-impact excitation cross sections in the field-free condition.

2.6.2. Electron momentum correlation between the two ejected electrons. Besides the total double ionization yields versus peak laser intensities, NSDI has also been investigated experimentally by measuring the ion momentum distributions in the direction of laser polarization, or, more precisely, by measuring the correlated momentum distributions of the two ejected electrons along the polarization axis. Such measurements have been reported in [74, 75]. In a recent paper, Chen *et al* [71] have applied the QRS model to this problem. For this purpose, triply differential cross sections from field-free electron-impact ionizations (often called the (e, 2e) process) must be calculated. Since these collisions occur in the laser field, equations (5) should be applied to the momentum of each electron as it exits from the laser field. The details are not given here. We only point out that the correlated electron spectra measured by Staudte *et al* [74] (figure 16(d)) can be explained only if the electron–electron interaction is included explicitly when calculating the momentum distributions of the two outgoing
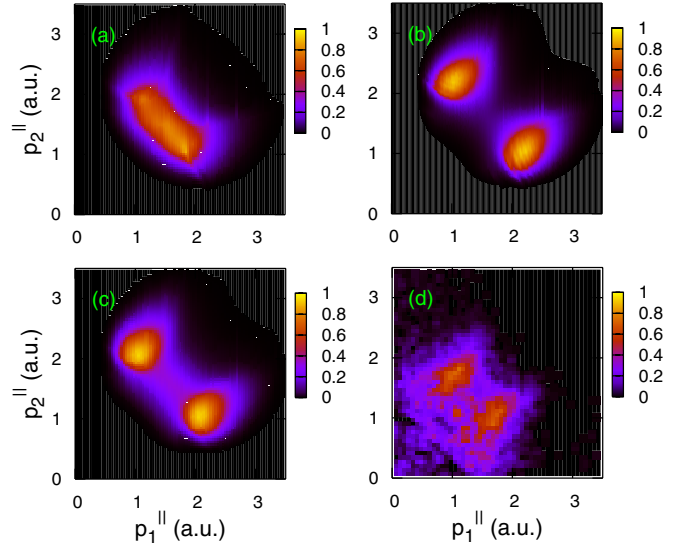
Figure 16. Momentum spectra of the two outgoing electrons in the nonsequential double ionization of He in an intense laser field with the wavelength of 800 nm and peak intensity of 4.5×10^{14} W cm^{-2} at the laser focus. Shown are the momentum components along the polarization axis for each electron and only the first quadrant is displayed. The spectra in the third quadrant are obtained through an inversion with respect to the origin. The experimental data from [74] are shown in (d) except that contributions from excitation followed by ionization by lasers have been removed, as explained in [71]. The finger-like feature in the experimental data is shown to result from the electron–electron repulsion between the two outgoing electrons. (a) shows that the finger-like structure does not appear if the Coulomb repulsion between the two continuum electrons is not included. (b), (c) demonstrated that the finger-like feature appears when electron–electron interaction is included in the final-state wavefunction. See the text.

electrons in the (e, 2e) process. In [71], this conclusion is drawn by considering wavefunctions of the two outgoing electrons with varying degrees of approximation. Assuming that the final state wavefunction of the two electrons are represented by an antisymmetrized product of two Coulomb wavefunctions (the P-CC model), the predicted momentum correlation spectra are shown in figure 16(a). This result does not look like the experimental data shown in figure 16(d). If the final state wavefunction is expressed as the product of three Coulomb functions (the P-CCC model)—one Coulomb function for each electron due to electron–nucleus interaction and another Coulomb wavefunction for the electron–electron interaction—then the predicted momentum correlation, as shown in figure 16(b), does reproduce the finger-like structure observed in the experiment. In figure 16(c), the result obtained from the DS3C model is shown. In DS3C, dynamic screening (DS) between each pair of charges (3C) has also been included. The DS3C model only modifies the calculated spectra slightly and is also in good agreement with experimental data. Based on these results one can draw the conclusion that the Coulomb repulsion between the two outgoing electrons is essential for the appearance of the finger-like structure observed by Staudte *et al* [74]. To fully explain the whole correlation spectra between the two electrons, contributions from the indirect processes, i.e. electron-impact excitation followed by

J. Phys. B: At. Mol. Opt. Phys. **43** (2010) 122001

Topical Review

tunnelling ionization from the excited states, should also be included. As shown in [76], the electron momentum spectra from the indirect processes cover the lower momentum region and thus do not affect the finger-like structure discussed in figure 16.

Not all the NSDI processes require the full treatment of electron–electron interaction. For example, the recoil-ion momentum spectral distribution in NSDI is mostly determined by the returning wave packets. Thus the ion momentum spectra of Ar^{2+} have been used to determine the carrier-envelope phase of few-cycle pulses, see [58].

2.7. Quantitative rescattering theory for HHG

2.7.1. High-order harmonic generation and photo-recombination. According to the rescattering model, HHG occurs when the returning electrons photo-recombine with the parent ions, with the emission of high-energy photons. Photo-recombination is the time-reversed process of photoionization. With the success of the QRS model for HATI and NSDI, one may anticipate a relation similar to equation (9) for HHG. Thus, within the QRS model, the *complex* laser-induced dipole is written as

$$|D(\omega)|\, e^{i\phi(\omega)} = |W(E)|\, e^{i\eta(E)} |d(\omega)|\, e^{i\delta(\omega)}, \qquad (14)$$

where ϕ and η are the phases of the harmonic and the returning electron wave packet $W(E)$, respectively, and d and δ are the amplitude and phase of the photo-recombination transition dipole. The electron energy E is related to the emitted photon energy by $E = \omega - I_p$, with I_p being the ionization potential of the target. Note that for convenience we denote the wave packet *amplitude* as W, whereas it was denoted as $|W|^{1/2}$ in equation (9) for HATI, up to a phase factor. (Complex scattering amplitude can also be calculated for HATI electrons, but so far there are no experimental measurements which probe its phases.)

To check the validity of the QRS ansatz in equation (14), in [77] HHG spectra from Ne and from a scaled hydrogen atom were calculated by solving numerically the TDSE in the same laser pulse. The Ne target again is treated within a single active electron model and the charge of the scaled hydrogen was chosen such that its 1s binding energy is the same as the 2p binding energy of Ne. Such a choice ensures that the HHG cutoffs from the two targets are identical. Photoionization amplitudes for Ne and for scaled H are also calculated. From equation (14), a wave packet (i.e. the square of the amplitude) for each target can be obtained. The two wave packets are compared in figure 17. It is clear that they are essentially identical over a range of photoelectron energies (up to an overall normalization factor, reflecting the difference in the ionization rates for the two targets). In figure 17, the wave packet from the SFA (or Lewenstein model) is also quite close to the ones from solving the TDSE (after it is normalized at the cutoff at 67 eV). Note that in the SFA, the transition dipole is calculated using plane-wave approximation. These results illustrate that the wave packets obtained through equation (14) are independent of the targets (note that H and Ne have different orbital symmetry) and to a good approximation, the wave packet can be obtained from the SFA.
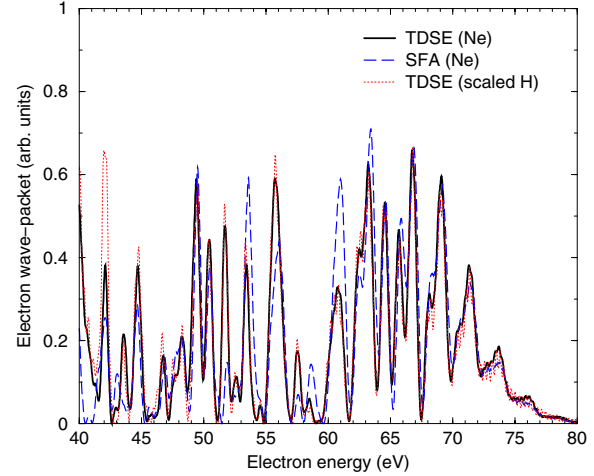

Figure 17. Comparison of the returning electron wave packet extracted from equation (14), obtained by solving the TDSE and from the SFA for Ne, and from solving the TDSE for a scaled atomic hydrogen. The three results are normalized near the cutoff at 67 eV.

2.7.2. Extracting photoionization cross sections and phases of transition dipole matrix elements from HHG. For the purpose of testing the accuracy of QRS, we will assume that the magnitude and phase of the transition dipole for scaled hydrogen atom are known exactly. If the HHG of Ar and of the scaled H are calculated from the TDSE under the same laser pulse, then the magnitude and the phase of the transition dipole for Ar can be extracted by comparing the HHG spectra of the two targets using equation (14). Furthermore, the results should be independent of laser intensity or wavelength. This has been carefully checked in [77, 34] and the results for Ar and Xe are shown in figure 18. For the magnitude, photo-recombination *differential* cross sections are shown. The symbols correspond to the data extracted from the calculated HHG spectra using different wavelengths or intensities. It is noted that for photon energies between 30 and 80 eV, the photo-recombination cross section for Ar is rather smooth with a minimum near 45 eV. The minimum is called a Cooper minimum [78] and its position is sensitive to the model potential used. For Xe in the same photon energy range, the photo-recombination cross section drops monotonically by more than a factor of 50. Note that near the Cooper minimum the phase of the transition dipole moment changes rapidly, see figure 18(c). Overall, the extracted cross sections and phases agree very well with the results obtained directly from photoionization calculations.

A few general remarks: to extract the photo-recombination cross section and phase of the transition dipole from the intensity and the phase of HHG, we typically perform a coherent average of the laser-induced dipole moments over ±5% of the laser peak intensity. This is approximately equivalent to including the macroscopic propagation effect and removes the contribution from long trajectories [79]. Also note that the QRS model is more accurate near the cutoff; thus, to retrieve results such as those shown in figure 18 over a broad range of energy, it is preferable to use different laser intensities and wavelengths so that for each measurement only
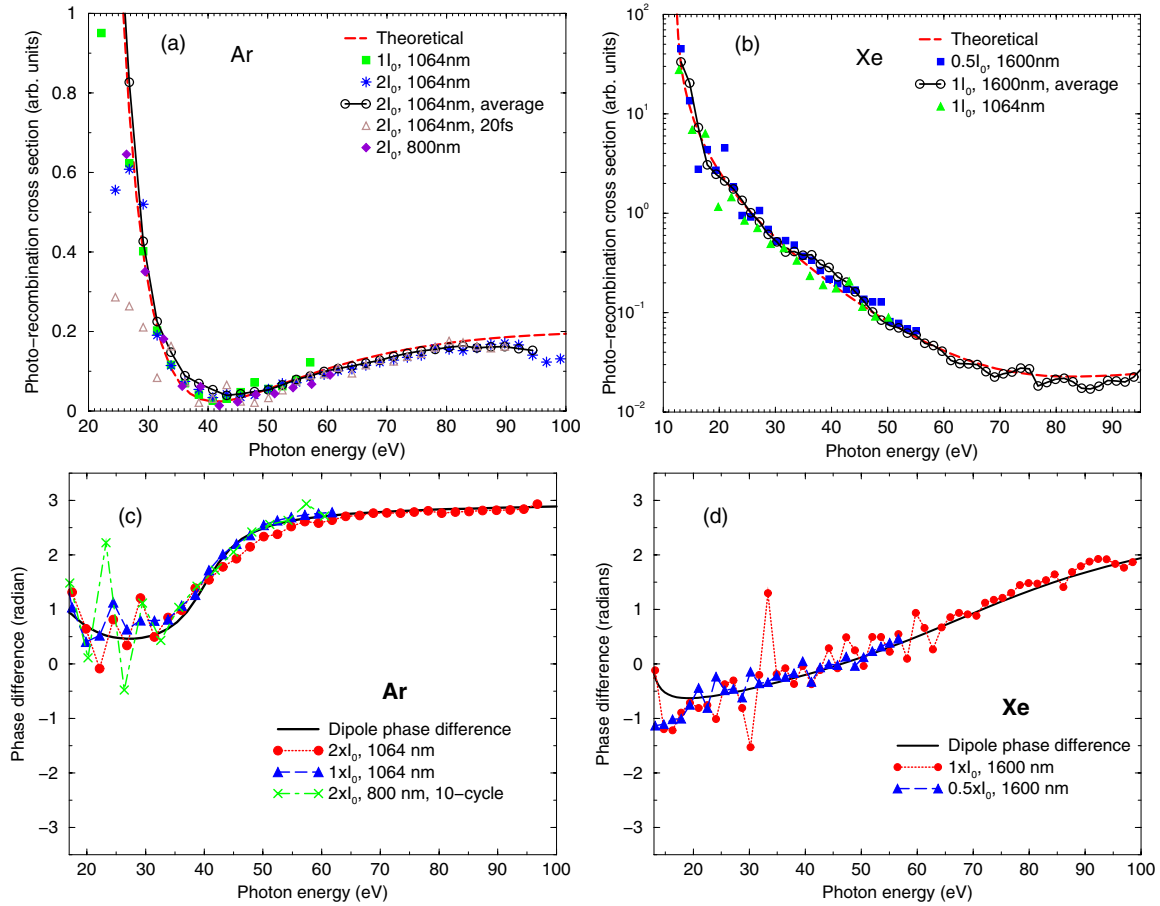
Figure 18. Extracted photo-recombination differential cross sections and phases from the HHG spectra as compared with the ones obtained directly from photoionization calculations for Ar and Xe. The phase relative to the scaled hydrogen are shown ($I_0 = 10^{14}$ W cm^{-2}). The parameters of the lasers used are indicated in the figure.

the harmonics that are relatively close to the cutoff are used. This is especially true for the phase retrieval, see, for example, figures 18(c) and (d).

2.7.3. Macroscopic propagation of HHG spectra. Experimental HHG spectra are the result of dipole radiation emitted from all the atoms within the interaction volume. The radiation from these atomic dipoles is generated coherently as it propagates in the medium. To compare with experimental HHG spectra, macroscopic propagation effects should be included in the theoretical simulation. The general theory of macroscopic propagation of HHG has been reviewed recently by Gaarde, Tate and Schafer [80]. In [81] the effect of HHG propagation in the low laser intensity and dilute gas limit was examined. Under such conditions, it was shown that the 'macroscopic' QRS model is still valid, similar to equation (11) for the volume-integrated HATI spectra. In figure 19, the extracted 'macroscopic' wave packets for scaled H and Ar targets under the same laser conditions are shown. For figures 19(a)–(c), the Ar jet was placed at 2, 2 and 1.5 mm after the focus and laser intensities are 1.5, 1.25 and 1.5×10^{14} W cm^{-2}, respectively. By changing the gas jet position with respect to the focus of the laser, different macroscopic wave packets are obtained, but the resulting wave packets are nearly independent of the targets. A similar check has been made for

the phase of the HHG, see [81] (especially figure 4). We thus draw the conclusion that one can extract the magnitude and phase of the transition dipole from experimental HHG spectra under favourable conditions.

The effect of macroscopic propagation on HHG is a very important topic for the generation of XUV and soft x-ray light pulses [82–84], as well as in attosecond pulse generation [80]. Most of the simulations are based on atomic dipoles calculated using the SFA. In view of the limitation of the SFA, such simulations cannot be compared quantitatively with experimental observations. In the future, the atomic dipoles should be calculated using the QRS model and fed into the propagation equation. We note that the dependence of HHG yields on the gas pressure and focusing conditions has been reported recently [85].

Before leaving this topic, we comment that there has been much interest (and confusion in the literature) in the position of Cooper minimum in the HHG spectra of Ar recently. According to QRS, the position of the Cooper minimum for HHG in Ar should not vary with laser intensity, nor with laser wavelength. This prediction is consistent with the experimental results of [86] where the position was found to be independent of the laser intensity. More recently, HHG measurements carried out using different wavelengths also showed that the Cooper minimum stays at the same position,
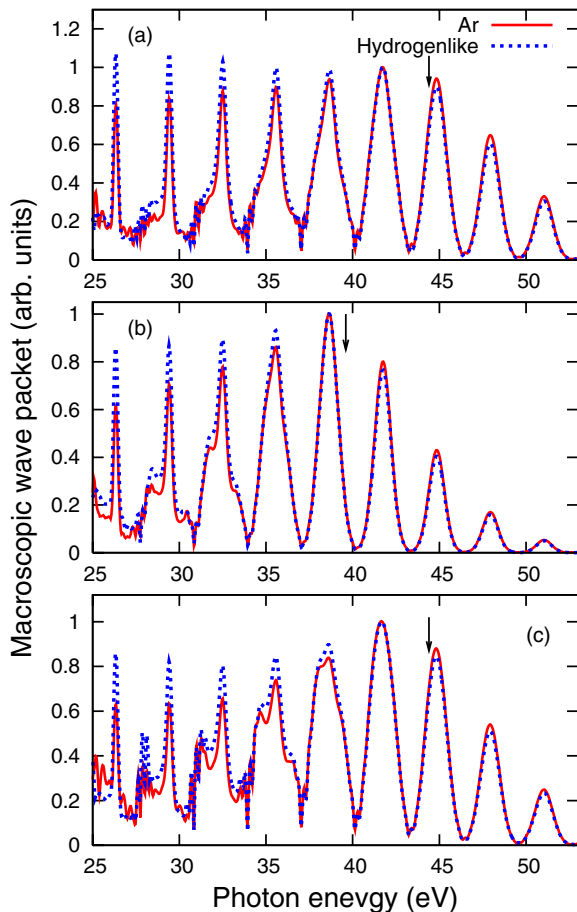
Figure 19. Macroscopic electron wave packets extracted from the macroscopic HHG spectra from Ar and scaled hydrogen for a gas jet located at 2, 2 and 1.5 mm after the focus and laser intensities of 1.5, 1.25 and 1.5×10^{14} W cm^{-2}, respectively. The figures illustrate that the macroscopic wave packets are independent of the target, but change with the focusing condition of the laser.

at about 51 eV [87]. We stress that in HHG, the position of the Cooper minimum has to do with the minimum in the *differential* dipole transition amplitude (at zero degree with respect to the polarization direction). This position can differ slightly from the position observed in photoionization of Ar [88] where it refers to the minimum in the total cross section. Additional complications occur in HHG since the propagation effect can change the relative strength of different harmonics [85]. Theoretically, to predict accurately the position of the Cooper minimum the dipole transition matrix element should be calculated using the many-electron model, not the single-electron models that have been used so far for HHG of Ar. In addition, the transition dipole matrix element is a complex number. Near the Cooper minimum the phase jump is not π in general; see, e.g., figure 18(c). A π phase jump occurs only when the continuum wavefunction is approximated by a plane wave, such as in the SFA.

2.8. Formal derivation of QRS for model atomic systems

We have presented a theoretical analysis and numerical evidence that support QRS for HATI, NSDI and HHG

processes in atomic targets. Conceptually, QRS can be thought of as a quantum version of the rescattering theory [11, 12], or an extension of the three-step model used by Itatani *et al* [19] which was based on the SFA. Following the initial work of Morishita *et al* [34] several attempts have been made to analytically derive the factorization formula of QRS, see equations (9) and (14).

Based on the time-dependent effective range theory together with the Floquet theory, Frolov *et al* [89, 90] showed that for monochromatic lasers, in the tunnelling regime the HHG and HATI spectra can be factorized as a product of three terms, namely the ionization part, the propagation part and the photo-recombination cross section or elastic scattering cross section, respectively. The first two terms give the returning electron wave packet. Within the effective range theory an active electron in the atom is assumed to be bound by a short-range potential. Thus, it is the derivation of the factorization used by Itatani *et al* [19]. We emphasize that there is no formal derivation so far of the factorization formula of QRS for real atomic systems which should include a long-range Coulomb potential.

In [91], Cerkic *et al* also presented a derivation of the factorization formula for the BRR, i.e. electrons returning with maximum kinetic energy of $3U_p$, and showed that the cross sections in the first-order Born approximation can be factored out. Their theory is based on a heuristic extension of the quantum orbit theory in order to account for the interaction of the returning electron with the parent ion.

Another derivation of the factorization formula has been reported recently by Tolstikhin *et al* for a 1D zero-range potential model [92]. This theory is an asymptotic expansion in terms of the adiabatic parameter, defined as the ratio of the atomic time scale with respect to the laser period. It was shown that *exact* laser-free scattering of the target atom can be factored out from the HATI spectra in the adiabatic limit.

Among all of these analytical derivations, the oscillating structure of the spectra is described by the Airy function [89–92]. The Airy function comes from the interference between the wave packet of the long and short trajectories in the semiclassical treatment of the rescattering process. Thus, the validity of the factorization is related to the adiabaticity, or the tunnelling ionization mechanism, in the interaction of an infrared laser pulse with atoms and molecules. The latter of course is the basis of the rescattering model, i.e. the starting point of the QRS theory. On the other hand, the region of validity of the QRS model seems to be broader than the underlying assumptions used in these analytical theories.

3. Strong-field rescattering physics for molecular targets

3.1. QRS model for HHG from aligned molecules

In this section we extend the QRS model to molecular targets. Unlike atomic targets, where within the single active electron approximation one can always use solutions of the TDSE to test the model, there is no such luxury with molecular targets. Few realistic TDSE calculations have been attempted for molecular

J. Phys. B: At. Mol. Opt. Phys. **43** (2010) 122001

Topical Review
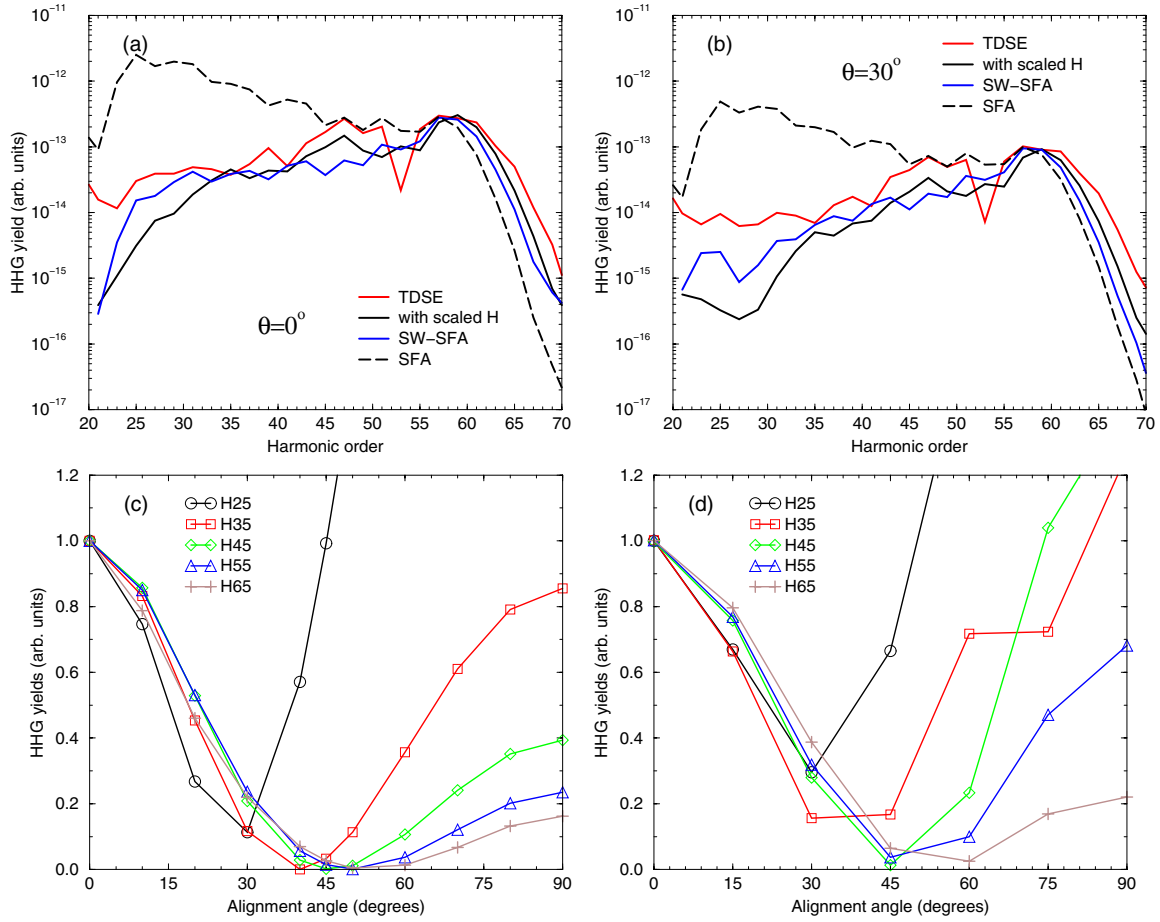
Figure 20. (a) and (b) Comparison of the HHG spectra of molecular ion H_2^+ from the TDSE, QRS and SFA at the alignment angle $\theta = 0°$ and $30°$, respectively. (c) and (d) Alignment dependence of some selected harmonics from the QRS and the TDSE, respectively.

targets except for HHG from H_2^+ ions [93–95]. In [96] it was shown that HHG spectra obtained from QRS are in agreement with these TDSE results. Fortunately, for molecules there are quite a few HHG experiments [97–102] from aligned molecules. To use QRS for the HHG of molecules, the major new ingredients needed are the tunnelling ionization rates and the transition dipole moment for aligned molecules. The latter are the same matrix elements that have been routinely calculated in molecular photoionization. Advanced computational methods developed over the last three decades can be used for this purpose. For the alignment dependence of tunnelling ionization rates, the MO-ADK theory of Tong *et al* [103, 104] is used.

3.1.1. Testing QRS for HHG from H_2^+ against TDSE results. In the last few years, HHG spectra by infrared laser pulses from H_2^+ fixed in space have been calculated by solving the full-dimensional TDSE equations in [93–95]. These results offer a chance for us to test the prediction of QRS for the HHG spectra on the simplest molecular target [96].

There are two ways to calculate HHG from a fixed H_2^+ ion (meaning that the two nuclei are kept frozen in space) using QRS [77]. One is to calculate the wave packet from SFA for H_2^+ directly. In [77] this is called SW-SFA where SW implies that the recombination transition dipole is calculated using

the exact scattering wavefunction, such as that used in the calculation of photoionization cross section of fixed-in-space H_2^+. The other way is to use a scaled hydrogen which has the same ionization energy as the vertical ionization energy of H_2^+ at the equilibrium distance. To account for the dependence of tunnelling ionization rates on the alignment angle—the angle θ between the molecular axis and the laser polarization axis—we use the MO-ADK theory.

The HHG spectra calculated using QRS are compared to those from the SFA and from the TDSE for alignment angles of $0°$ and $30°$ in figures 20(a) and (b), respectively. The results are normalized at the cutoff harmonic. Note that there is general agreement between the two QRS results with the TDSE results, except that the TDSE results are less smooth versus alignment angles and harmonic orders—perhaps a consequence of numerical instability. The predictions from the SFA generally are adequate near the cutoff (where it is normalized to the TDSE), but deviate significantly from the correct results for harmonics farther away from the cutoff region. In figures 20(c) and (d) the harmonic yields versus alignment angle are shown, by comparing the QRS (the SW-SFA model) results with the predictions from the TDSE. The general trend appears to be quite similar, except that the TDSE results show less smooth variation with the change of alignment angle.

Based on such comparisons, we conclude that the QRS model works well for the H_2^+ molecular ion. The next tests will have to be directed at HHG spectra from aligned molecules that have been investigated experimentally. According to QRS, we would need photo-recombination transition dipole matrix elements which can be obtained from photoionization codes.

3.1.2. Photoionization transition dipole moments from fixed-in-space molecules.

Photoionization of molecules has been studied theoretically and experimentally for over more than four decades [105, 106]. The differential photoionization cross section can be expressed in the general form [107]:

$$\frac{d^2\sigma^I}{d\Omega_{\mathbf{k}}d\Omega_{\mathbf{n}}} = \frac{4\pi^2\omega k}{c}|d_{\mathbf{k},\mathbf{n}}(\omega)|^2, \tag{15}$$

where $\omega = k^2/2 + I_p$ is the photon energy, $\mathbf{k}$ the momentum of the ejected photoelectron and $\mathbf{n}$ the direction of photon polarization.

The main task in photoionization theory is the calculation of the transition dipole matrix element

$$d_{\mathbf{k},\mathbf{n}}(\omega) = \langle \Psi_i | \mathbf{r} \cdot \mathbf{n} | \Psi_{f,\mathbf{k}}^- \rangle, \tag{16}$$

where Ψ_i is the initial bound state and $\Psi_{f,\mathbf{k}}^-$ is the final continuum state. Within a single-channel approximation, the final state can be written as

$$\Psi_{f,\mathbf{k}}^{(-)} = \mathbf{A}\left[\Phi\phi_{\mathbf{k}}^{(-)}\right], \tag{17}$$

where Φ is the correlated electron wavefunction of the parent ion, $\phi_{\mathbf{k}}^{(-)}$ is the wavefunction of the continuum electron and $\mathbf{A}$ is the antisymmetrization operator. The continuum wavefunction is expanded in terms of partial waves as

$$\phi_{\mathbf{k}}^{(-)}(\mathbf{r}) = \left(\frac{2}{\pi}\right)^{1/2} \sum_{l=0}^{l_p} \sum_{m=-l}^{l} \mathrm{i}^l \phi_{klm}^{(-)}(\mathbf{r}) Y_{lm}^*(\Omega_{\hat{k}}), \tag{18}$$

where an infinite sum over the partial waves l has been truncated at $l = l_p$. The transition dipole can then be conveniently expanded in terms of spherical harmonics as

$$d_{\mathbf{k},\mathbf{n}}(\omega) = \left(\frac{4\pi}{3}\right)^{1/2} \sum_{lm\mu} d_{lm\mu} Y_{lm}^*(\Omega_{\mathbf{k}}) Y_{1\mu}^*(\Omega_{\mathbf{n}}), \tag{19}$$

where the partial wave matrix elements are given by

$$d_{lm\mu}(\omega) = \langle \Psi_i | r_\mu | \phi_{klm}^- \rangle, \tag{20}$$

with

$$r_\mu = \begin{cases} \mp(x \pm \mathrm{i}y)/2^{1/2} & \mu = \pm 1, \\ z & \mu = 0. \end{cases} \tag{21}$$

To simplify the angular integration, a single-centre expansion approach is used in our calculations to evaluate all required matrix elements

$$F(\vec{r}) = \sum_{l=0}^{l_{\max}} \sum_{m=-l}^{l} f_{lm}(r) Y_{lm}(\theta, \phi), \tag{22}$$

where the origin is taken at the centre of mass of the molecule and we typically choose $l_{\max} = 85$. In our calculations the initial bound state Ψ_i is obtained from the MOLPRO [24] within the valence complete-active-space self-consistent field (CASSCF) method. The target part Φ of the final state is given by a valence complete-active-space configuration interaction wavefunction using the same orbitals that are used in the initial state. The continuum wavefunction is calculated by using the iterative Schwinger variational method [107]. For harmonic emission with polarization along the laser polarization direction, only the differential cross sections for $\mathbf{k} \parallel \mathbf{n}$ are needed.

Calculation of photoionization transition dipole matrix elements with different degrees of accuracy is a specialized subject in its own right. While many popular quantum chemistry packages are available for obtaining ground state wavefunctions of molecules, the calculation of continuum wavefunctions can only be done by collaborating with experts in the field. A short summary of the calculation of dipole matrix elements for linear molecules has been given in [36], but the details are outside the scope of this review. Note that transition dipole matrix elements are complex numbers; thus, they are characterized by their magnitude and phase. The latter will be reflected in the phase of the HHG.

3.1.3. HHG from aligned molecules.

In general, gaseous molecules are randomly oriented in space. When a molecule is placed in a short laser pulse of moderate intensity, a rotational wave packet is generated. After the pulse is over, the rotational wave packet will rephase at intervals characteristic of rotational periods [108]. During these rotational revivals, the angular distributions of the molecules are preferentially aligned or anti-aligned with respect to the pump laser's polarization axis. Using lasers to align molecules is an active area of research. For linear molecules the degrees of alignment can be calculated using a rigid rotor model. The alignment can also be determined using the Coulomb explosion technique with an intense circularly polarized light. The calculated or measured time-dependent angular distribution of these aligned molecules is expressed as $\rho(\chi, t)$ where χ is the angle between the molecular axis and the laser polarization axis of the pump beam. If the laser parameters and temperature of the gas are known, then $\rho(\chi, t)$ can be calculated, see the review [108] or section II.F of [36].

To generate high-order harmonics from aligned molecules, experimentalists use a more intense short probe pulse which is applied to the gas at different delay times when the molecules are preferentially aligned or anti-aligned, or at a fixed delay time but changing the direction of the probe laser polarization with respect to the pump laser polarization. In recent years, many such measurements have been reported from a number of laboratories. These measurements reported HHG yields versus the alignment angles or time delays. More recently, the phases and polarizations of the harmonics have also been reported. For more details on the measurements, readers are referred to the experimental publications [20, 100–102]. In this review, we will focus on CO_2 and N_2 targets as these two species have been examined in many experiments.

J. Phys. B: At. Mol. Opt. Phys. **43** (2010) 122001

Topical Review

We will mostly compare calculations based on the QRS model with these measurements.

In applying QRS to HHG from fixed-in-space molecules where the molecular axis makes an angle θ with respect to the probe laser's polarization axis, the induced dipole $D(\omega, \theta)$ can be expressed as

$$D(\omega, \theta) = W(E, \theta) d(\omega, \theta), \tag{23}$$

or more explicitly

$$|D(\omega, \theta)| \, e^{i\varphi(\omega, \theta)} = |W(E, \theta)| \, e^{i\eta(\omega)} |d(\omega, \theta)| \, e^{i\delta(\omega, \theta)}. \tag{24}$$

Here $d(\omega, \theta)$ is the photo-recombination transition dipole, ω the photon energy of the emitted harmonic, E the energy of the returning electrons, with $E + I_p = \omega$, where I_p is the ionization potential of the target, and $|W(E, \theta)|^2$ gives the 'flux' of the returning electrons. In equation (24), the phase φ of the harmonics is the sum of the phase of the wave packet η and the phase of the PR transition dipole δ. The HHG signal is proportional to $|D(\omega, \theta)|^2$. As in the case of atomic targets, the wave packet $W(E, \theta)$ can be calculated using the Lewenstein model for each molecular alignment angle θ. Alternatively, since the flux of the returning electrons depends on the tunnelling ionization rate, which in turn depends on the alignment angle, we can write

$$|W(E, \theta)|^2 = N(\theta) \times |\tilde{W}(E)|^2, \tag{25}$$

where $N(\theta)$ is proportional to the θ-dependence of the ionization rate. We obtain $N(\theta)$ either from the MO-ADK theory or from the molecular SFA1. Strictly speaking, $N(\theta)$ is related to the ionization probability for electron emission along the laser polarization direction [36]. By using equation (25) the wave packet can also be obtained from the Lewenstein model or from numerical solution of the TDSE for a reference atom chosen such that it has the same ionization potential as the molecule. We have found that the two approaches give quite comparable results [21, 36]. Recombination transition dipole is calculated using the Schwinger variational method developed by Lucchese and collaborators [107, 109–111], as described in the previous subsection.

To compare with experiments, induced dipoles from fixed-in-space molecules are coherently convoluted over the alignment distribution of the molecules. If the pump and probe lasers have polarizations along the same direction, the total induced dipole is calculated from

$$\bar{D}(\omega, t) = 2\pi \int_0^\pi D(\omega, \theta) \rho(\theta, t) \sin\theta \, d\theta, \tag{26}$$

If the two polarizations are not parallel, then a more complicated calculation must be carried out, see section II.F of [36].

3.1.4. HHG spectra from aligned CO_2—QRS and experiments. High-order harmonics from aligned molecules have been investigated since 2005. In particular, HHG from CO_2 molecules have been investigated by many experimental groups. Besides the QRS theory, HHG from CO_2 has also been studied theoretically in [113–115], which will be covered in a separate subsection below. We also mention that earlier

calculations using the standard SFA theory [48, 116, 117] agree only qualitatively with experimental measurements.

Below we walk through the steps involved in using the QRS theory for the calculation of HHG spectra from CO_2 molecules, following equation (24). We will then compare the predictions with experimental results. A more detailed explanation can be found in [36].

1. *Dependence of tunnelling ionization rates on the alignment angles.* As shown in [118] the molecular structure parameters needed in the MO-ADK theory for calculating tunnelling ionization rates of CO_2 originally given in [103, 116] were not very accurate. Using the new parameters obtained in [118], the new MO-ADK rates for ionization from the HOMO are in good agreement with calculations based on the time-dependent density functional theory (TDDFT) [119] and with those obtained from solving the TDSE where the many-electron problem has been reduced to an effective one-electron model problem [120]. However, while all of these theoretical calculations are in good agreement with each other, they are in disagreement with the experimental $N(\theta)$ reported in [121]. On the other hand, at lower laser intensities all of these theoretical calculations for $N(\theta)$ are in better agreement (see [118]) with the experimental data reported in [122].

   In [113–115], it was argued that HOMO-1 and HOMO-2 orbitals also contribute to the HHG spectra of CO_2. We thus also obtained molecular structure factors for these orbitals [104] to obtain the MO-ADK rates. In figure 21(a), these rates are compared with the most recently reported rates from [123], by normalizing the peak HOMO rate between the two theories. There is a very close agreement between the two theories for the HOMO. For HOMO-1 and HOMO-2, the alignment dependence from the two theories are very similar, but the rates from [123] for the inner orbitals are a few times larger. A similar comparison is made in figure 21(b) between the MO-ADK rates and the rates used in [113, 114]. Their alignment dependence for each orbital is not quite the same as in the MO-ADK theory. Still, the discrepancy between the theories and the experimental data of [121] is more substantial at this time.

2. *Calculation of the recolliding electron wave packet $W(E, \theta)$.* As discussed in section 3.1.3, there are two ways to obtain the wave packets. One can use the SFA (or Lewenstein model) or one can solve the TDSE for a reference atom. Since Kr has nearly the same ionization potential as CO_2, it can be conveniently used as a reference atom. At low intensities ($\sim 10^{14}$ W cm^{-2}), these two methods gave nearly the same results. At higher laser intensities, the SFA is used to extract $W(E, \theta)$ so that the alignment dependence of the ground state depletion can be taken into account. The depletion is included in the standard manner as in [27], and its extension to molecular targets as in [48]. In [36, 124], the ionization rate from the molecular SFA (normalized to the MO-ADK result at 10^{14} W cm^{-2}) was used to account for the depletion since the alignment dependent rate from the 'old' MO-ADK
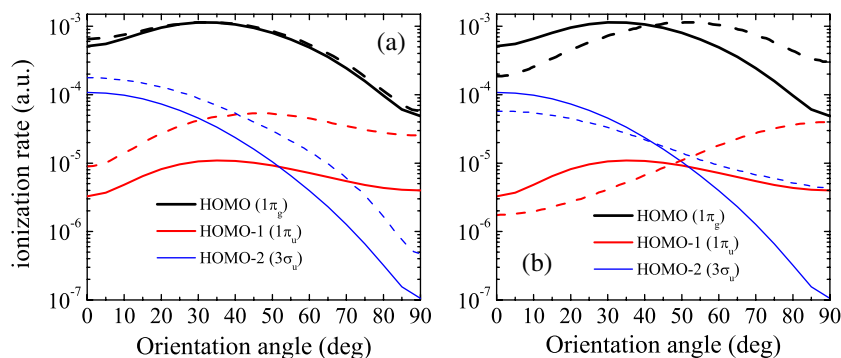
Figure 21. Ionization rates of HOMO, HOMO-1 and HOMO-2 of CO_2 at laser intensity of 1.5×10^{14} W cm^{-2}. The solid lines are from the MO-ADK and the dashed lines are from [123] (a) and from [113] (b).

[103, 116] was known to be inaccurate. As shown by Zhao *et al* [104], the alignment dependence of the newly determined MO-ADK rate agrees well with the prediction of molecular SFA.

3. *Calculations of complex photo-recombination dipole matrix elements*. Since photo-recombination and photoionization processes use the same dipole matrix element, we adopted established molecular photoionization theory and computer codes to generate the complex transition dipole $d(\omega, \theta)$. In practical applications, equation (16) is calculated with an accurate initial state wavefunction obtained from the MOLPRO code [24] within the valence CASSCF method. We use a single-channel approximation for the final state, where the target part is given by a valence complete-active-space configuration interaction wavefunction using the same orbitals that are used in the initial state. The continuum wavefunction of the photoelectron is expressed in terms of partial waves with up to $l_p = 11$. To simplify the angular integration a single-centre expansion is used to evaluate all required matrix elements. The centre of expansion is taken to be the centre of mass of CO_2 and spherical harmonics up to $l_{max} = 85$ are used. This photoionization package has been well tested for photoionization of molecules [107, 109].

4. *Comparison with experimental data*. In figure 22(a) we show the calculated differential photoionization cross sections (PICS) of CO_2 for fixed-in-space molecules. The molecules make an angle θ with respect to the polarization axis of the IR laser, and the photoelectron is ejected along the polarization axis of the laser (the direction of the recolliding electron). The phases of the transition dipole matrix elements, equation (16), are given in figure 22(b). These cross sections and phases correspond to the parallel polarization components of the harmonics, which in general are expected to be dominant when compared to the perpendicular polarization. In figure 22(a), the PICS at $\theta = 0°$ and $90°$ vanish due to the symmetry since the HOMO is a π_g orbital. We also note that the PICS has a minimum between $30°$ and $50°$ for the harmonics shown. These minima can be understood as the interference [112] from the

two atomic emitters. In general, the position of the minimum cannot be predicted by such a model. Near the minima of the PICS, the phase of the transition dipole undergoes rapid change, see figure 22(b), for θ between $30°$ and $50°$. Since the 'wave packet' is a smooth function of the harmonic order for 'long' pulses used in most of the experiments, the structure of HHG from molecules is governed by $N(\theta)$, shown in figure 21, and the transition dipoles and phases shown in figures 22(a) and (b). For comparison with experimental data, an average over the angular distributions of the aligned molecules is carried out. Figure 22(c) shows the effect of such an angular integration.

Here we will not address earlier experimental results [97, 98, 126, 127] even though they have generated a great deal of interest in this topic. Without going into the details, we summarize how the predictions of the QRS compared to recent experiments from different groups: (a) the intensities of the harmonic yields versus the alignment angles of the molecules, from [128], see figures 23(a) and (b); (b) the phases of the harmonics (with respect to Kr) for parallel and perpendicular alignment angles from [102], see figure 22(d); (c) the time evolution of the harmonic intensities and phases versus the time delay between the pump and probe pulses, from [101], see figures 23(c)–(f). For more detailed discussions on these results, refer to the figure captions and [36, 124]. Clearly the QRS predictions are largely in good agreement with these measured results.

3.1.5. Multiple orbital effects on the HHG spectra of N_2. In a recent experiment McFarland *et al* [129] reported the HHG spectra from N_2 where the alignment of the molecules is perpendicular to the driving laser polarization. They observed a peak in the HHG yield at the rotational half-revival and the harmonic order, where the peak appears, depends on the laser intensity. They interpreted the emergence of this maximum at the higher orders (instead of the minimum for the lower orders) as the signature of the HHG contribution from the HOMO-1. This interpretation was confirmed quantitatively using the QRS model by Le *et al* [130]. In figures 24(a) and (b) the tunnelling ionization rates from the HOMO, HOMO-1 and HOMO-2 orbitals of N_2 are calculated using the MO-ADK model for two laser intensities. In figures 24(c) and (d)
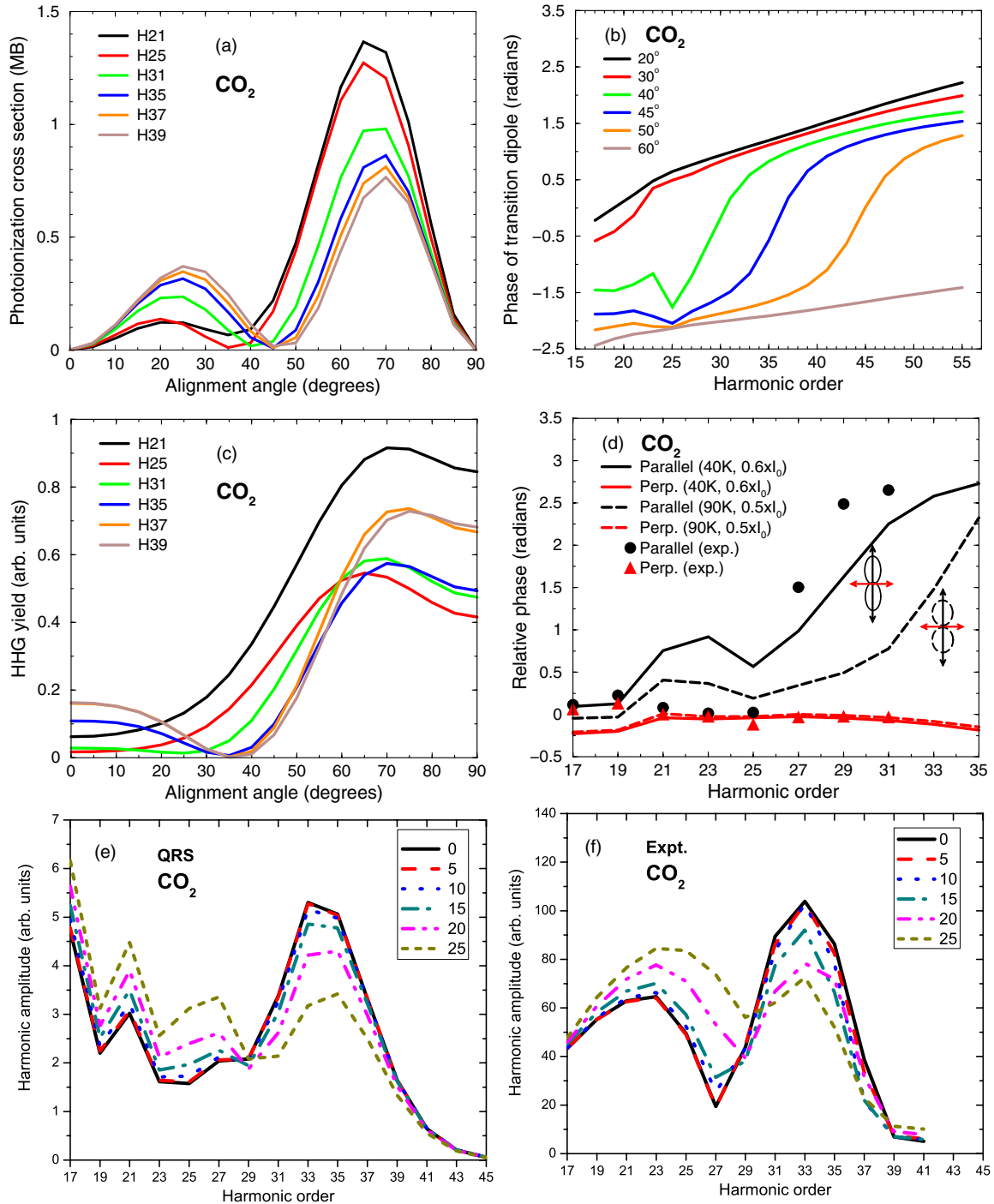
Figure 22. (a) and (b) Differential photoionization cross sections and the phase of the transition dipoles for CO_2 at few selected energies and alignment angles, respectively. (c) Harmonic yields as a function of the pump-probe angle. Convolution with the angular distributions of the molecules has been included. (d) Harmonic phase (relative to that from Kr) from parallel and perpendicular setups. The solid (or dashed) lines corresponds to the case of higher (or lower) degree of alignment. (e) and (f) Harmonic amplitudes from QRS and [128], respectively, versus the pump-probe angles. The experimental data have been renormalized to the Ar data under the same laser field.

we show the differential photoionization cross sections from the HOMO and the HOMO-1 versus alignment angles and photon energies. According to QRS, the HHG yield is proportional to the product of tunnelling ionization rate and the photoionization cross sections. From figures 24(a) and (b) clearly the HOMO-1 can become important for alignment angles near 90°, in part because the photoionization cross section from the HOMO-1 near 90° is a few times larger than from the HOMO. As laser intensity increases, the relative ionization rate from the HOMO-1 increases, as compared to the HOMO, thus further favouring the contribution from the HOMO-1. The HOMO-1 contribution is even more
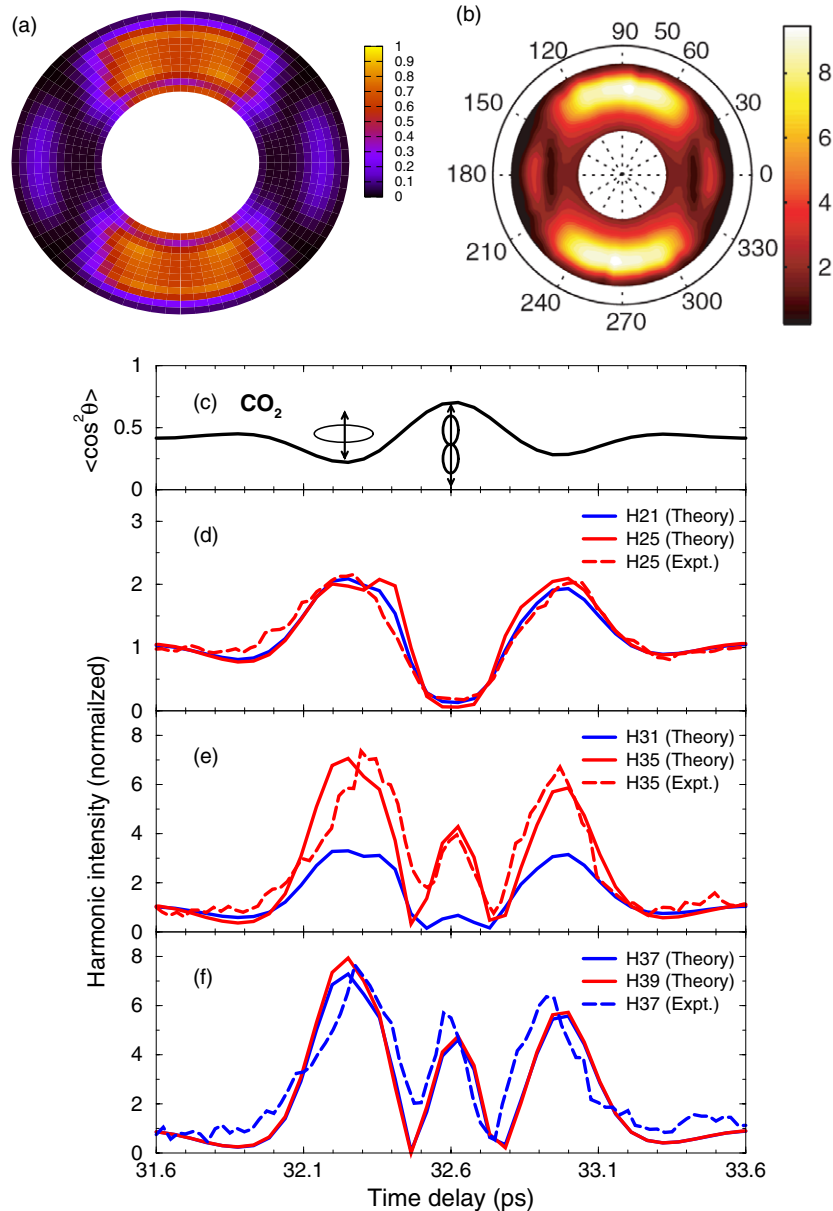
Figure 23. (a) and (b) Polar plot of harmonic yields for CO_2 from QRS and the experiments by Mairesse *et al* [128], respectively. The polar angle corresponds to the angle between the pump and probe polarizations. (d)–(f) Harmonic signal versus time delay near 3/4-revival for few selected harmonics. The dashed lines correspond to the experimental measurements by Zhou *et al* [101]. The degree of alignment $\langle \cos^2 \theta \rangle$ is also shown for reference (c).

pronounced near the HHG cutoff. Due to the different ionization potential, the cutoff energy for HHG from the HOMO-1 is 1.4 eV higher than from the HOMO. Putting these three factors together and carrying out the coherent convolution over the molecular alignment distribution at each time delay, the predictions of the QRS theory are shown in figures 24(e) and (f). Note that for the lower intensity shown in figure 24(f), H35 is already beyond the cutoff for both orbitals. The resulting HHG spectra are in good agreement with the experimental measurements by McFarland *et al* [129], shown in figure 24(g).

3.1.6. Polarization and ellipticity of HHG from aligned molecules. For atoms or unaligned molecular targets, due to

the symmetry, only the parallel polarization components of the harmonics are emitted. For aligned molecules, harmonic components perpendicular to the driving laser polarization are expected to be present in general [131]. Experimentally, HHG polarization measurements were reported only very recently [20, 128, 132, 133] for aligned N_2, O_2 and CO_2. Their results showed strong species dependence. In the measurements by Zhou *et al* [134] strong ellipticity in harmonic emission was found from strongly aligned N_2.

Theoretically, it has been noted already in [20] that simulation based on the SFA cannot quantitatively reproduce the polarization measurements. Furthermore, the SFA does not predict the ellipticity of the emitted harmonics. Within QRS, the induced dipole in equation (23) can be generalized to
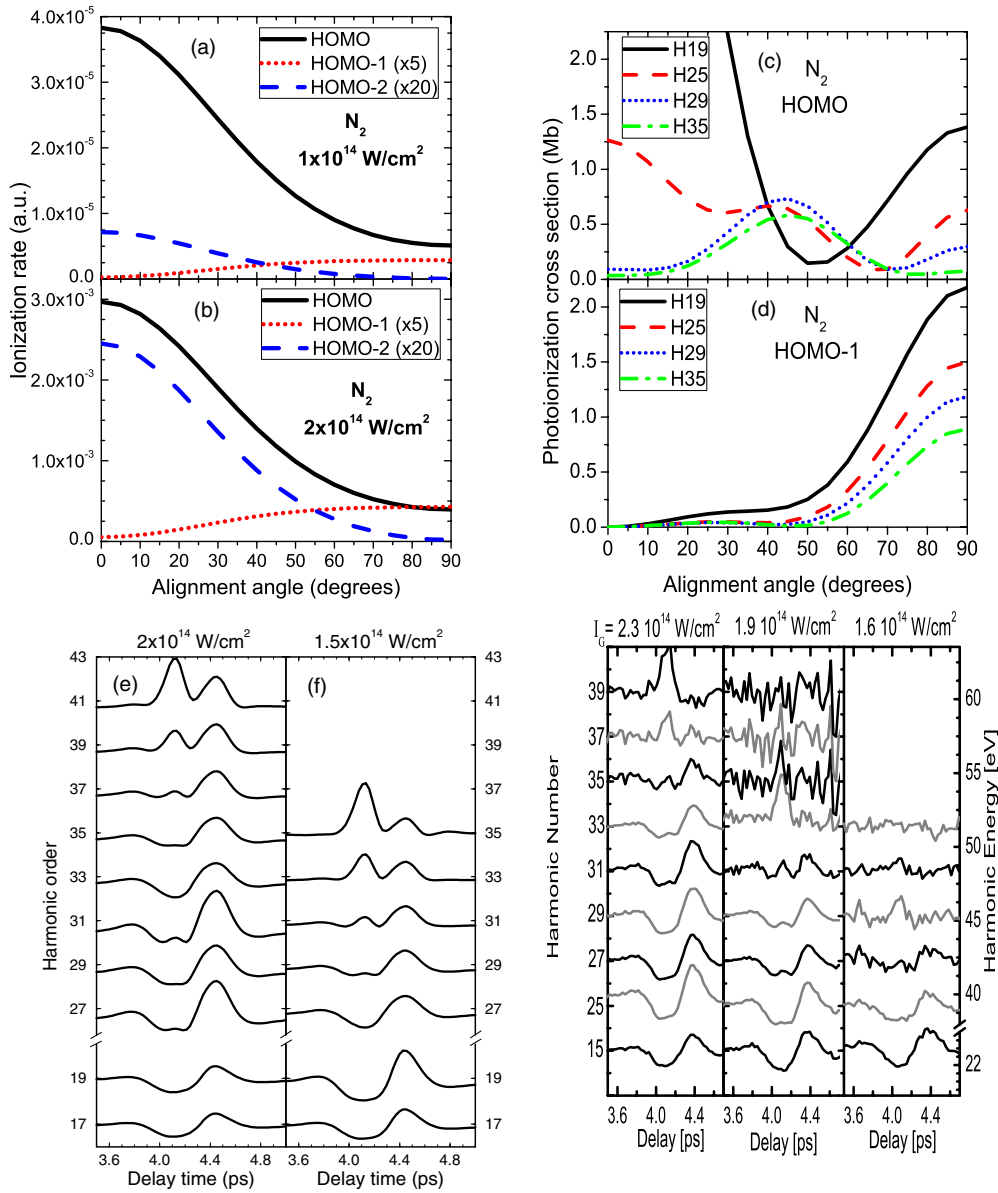
Figure 24. (a) and (b) Ionization rates from HOMO, HOMO-1 and HOMO-2 at laser intensities of 1×10^{14} and 2×10^{14} W cm^{-2}, respectively. The data from HOMO-1 and HOMO-2 have been multiplied by a factor of 5 and 20, respectively. (c) and (d) Differential photoionization cross sections from HOMO and HOMO-1, respectively, at some selected energies. (e) and (f) Theoretical HHG signals versus delay time near half-revival at laser intensities of 2×10^{14} and 1.5×10^{14} W cm^{-2}, respectively. (g) Experimental HHG signal versus delay time from [129].

calculate each HHG component separately. More specifically, the *same* returning electron wave packet can recombine with the parent ion to emit photon with polarization parallel or perpendicular to its motion, resulting in the two polarization components of the emitted harmonics. For comparison with experiments, induced dipoles $D_\parallel(\omega, \theta)$ and $D_\perp(\omega, \theta)$ from fixed-in-space molecules are coherently convoluted with the molecular alignment distribution [36, 131]. We note that this alignment 'phase-matching' tends to favour more the parallel component. These calculations within the QRS model have been carried out recently [135]. The results show strong species dependence of polarization states, in excellent agreement with experiments reported in [20, 134].

3.1.7. Alternative approach for HHG from aligned molecules. A similar scheme for calculating HHG from molecules has been used in [113–115] by generalizing an earlier theory of Ivanov *et al* [136]. This theory is also based on the rescattering picture except that it is expressed in the time domain. The laser induced dipole $D(t)$ is approximated as

$$\mathbf{D}(t, \theta) \propto \sum_{j, t_b} a_{\text{ion}, j}\,[t_b, \theta]\, a_{\text{prop}}\,[t, t_b, \theta]$$

$$\langle \Psi_{NT}(t, \theta)|\hat{\mathbf{d}}|\hat{A}\Psi_j A_j(t, \theta)\chi_{C,j}(t, k(t), \theta)\rangle + \text{c.c.} \quad (27)$$

where contributions from multiple orbitals have been explicitly included (each channel is labelled by j). In this equation, the
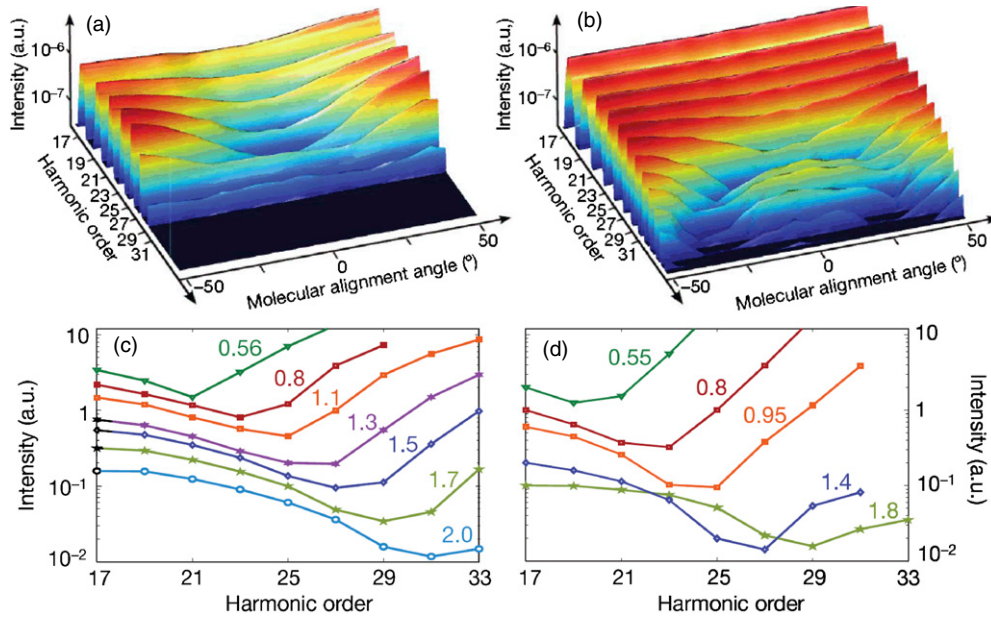
Figure 25. (a) and (b) measured harmonic signals from aligned CO_2 at laser intensities of 1.1×10^{14} and 1.8×10^{14} W cm^{-2}, respectively. (c) and (d) calculated and measured harmonic signals at an alignment angle $\theta = 0°$, respectively. The laser intensities are given in the labels (in units of 10^{14} W cm^{-2}). Taken from [113].

first amplitude under the summation describes the tunnelling ionization amplitude at time t_b when the electron is born into the continuum, and the second term is the amplitude of propagation of this electron in the laser field from t_b to t, when the electron recombines with the parent ion, and the last term is the transition dipole. The θ is the alignment angle of the molecule with respect to the laser polarization direction. Note that equation (27) is formally similar to QRS except in the time domain. However, the details of the calculations are different from QRS. In equation (27), the transition dipole includes field effects. In contrast, the transition dipole in QRS is independent of the laser field and is written in the energy domain. Another important difference is that the continuum electron wavefunction χ_C in equation (27) is calculated using the strong-field eikonal Volkov approximation [137]. For the details of this theory, the reader is referred to the supplementary information of [113].

The theoretical results from the above theory have been reported in [113, 114] for HHG from aligned CO_2 molecules. In [113] the theoretical harmonic yields at $\theta = 0°$ were compared with experimental data at different laser intensities. Their results are shown in figures 25(c) and (d). One can see that the harmonic yield shows minimum at certain harmonic order for each laser intensity. As the laser intensity increases, the minimum shifts to higher harmonics. In [113], contributions from the HOMO, HOMO-1 and HOMO-2 were found to be of comparable importance. According to their model, it is essential to take into account the ion dynamics coherently during the time interval between ionization and recombination. According to this theory, the HOMO alone cannot reproduce the experimental data (see [114]).

In contrast, the QRS model predicts similar HHG spectra (compare, for example, figures 22(c) and 23(a) with figures 25(a) and (b)), but with the contribution from the HOMO only.

We further comment that similar dynamics of the minimum in HHG spectra as a function of laser intensity can also be reproduced within the QRS. Here the contributions from the HOMO-1 and HOMO-2 only slightly affect the precise position of the minima. It is therefore highly desirable to understand the nature of this discrepancy between the two theories, probably by detailed comparisons between their predictions as well as with available and future experiments on other molecules. As the validity of the QRS model has been tested against the 'exact' numerical solution of the TDSE for atomic systems as well as for molecular ion H_2^+, it is interesting to see similar validity tests on equation (27), especially with the eikonal approximation for the transition dipoles.

3.2. HATI spectra from aligned molecules

For atomic targets, in section 2.4.2, we showed that it is possible to extract accurate elastic DCS at large angles from the HATI spectra. One should be able to do the same for molecular targets. Because of the multi-centre nature of molecules, theoretical calculations of elastic DCS are much more complicated. Experimentally, HATI spectra from isotropically distributed N_2 and O_2 molecules have been reported by Okunishi *et al* [138] and analysed by Busuladzic *et al* [139] using molecular strong-field approximation (the same as SFA2 defined in equation (2)). The HATI spectra of isotropic CO_2 have also been reported by Cornaggia [140] where the electron–CO_2^+ elastic DCS have been extracted at incident electron energies of 15 eV and 30 eV. In [141] HATI spectra from aligned N_2 and O_2 were reported. In the latter, the electron momentum distributions were measured on a plane perpendicular or parallel to the laser polarization axis.

To apply QRS to HATI spectra for molecular targets, one needs elastic DCS for electron collisions with molecular ions

that are fixed in space. While such computational tools are available, as will be addressed below, they have not been employed in actual calculations so far. We comment that the molecular strong-field approximation used in [139] and the two-centre interference model used in [141] are all based on treating continuum electrons as plane waves. With such simple models, the important structural properties of the target are left out.

We comment that electron–molecule collisions are the conventional tools for gas phase electron diffraction (GED) [142] for the determination of molecular structure. In section 4, we will discuss the potential of using HATI spectra for probing the structure of a transient molecule.

3.2.1. Elastic differential scattering cross sections for electron–molecular ion collisions. According to QRS, the HATI spectra from a molecule M can be used to extract the DCS at large scattering angles for $e^- + M^+$ collisions. For HATI spectra generated by a typical 800 nm laser, the energies of the returning electrons are in the order of 15–40 eV for peak laser intensity around 10^{14} W cm^{-2}. Electron–molecule collisions at low energies have many applications [143, 144] and many experimental and theoretical studies have been carried out in the past half a century. Computational packages using the R-matrix method [145], the finite-element R-matrix method [146, 147] and many others have been developed. These codes in general are written for randomly oriented molecules and are designed mostly for low-energy electrons. To make these codes useful for HATI studies, they have to be modified to electron collisions with aligned molecular ions and to higher collision energies. Such efforts are beginning to emerge, see [148]. Until such calculations become available it is difficult to apply QRS to the experimental HATI spectra reported so far [138, 140, 141].

3.2.2. Independent atom model for electron–molecule collisions. In the present review, our interest is whether the DCS obtained from HATI spectra can be used for the self-imaging of the target molecule. For this purpose, it is desirable that the theory for DCS be simple. In traditional GED, a beam of electrons with energies from tens to hundreds of keVs are aimed at randomly distributed molecules. The scattered electrons are measured in the forward directions and the DCS are calculated using the independent atom model (IAM) [149, 150]. In such cases, the radial distribution function of the molecule can be obtained by taking the inverse sine transform [142, 149, 151] of the scattering data. Here we examine whether IAM can be applied to electron collisions at lower energies, e.g. for energies near 100 eV. Such electrons have a de Broglie wavelength on the order of 1 Å.

In IAM, a molecule is modelled as consisting of a collection of individual atoms fixed at R_i. Let f_i be the complex scattering amplitude of the ith atom alone, the IAM assumes that the total scattering amplitude for a molecule fixed-in-space be expressed as

$$F(k, \theta, \varphi; \Omega_L) = \sum_i f_i \, e^{i q \cdot R_i}, \qquad (28)$$

where Ω_L is the angle between the molecular axis with respect to the direction of the incident electron, and $q = k - k_0$ is the momentum transfer. The incident electron momentum k_0 is taken to be along the z-axis. The scattering cross section is then given by

$$I_{tot}(\theta, \varphi; \Omega_L) = I_A + \sum_{i \neq j} f_i f_j^* e^{i q \cdot R_{ij}}, \qquad (29)$$

where $R_{ij} = R_i - R_j$ and $I_A = \sum_i |f_i|^2$. Here I_A is the incoherent sum of scattering cross sections from all the atoms in the molecule. The second term, I_M, is the molecular interference term. For electron scattering from a sample of randomly distributed molecules, the above expression is averaged over Ω_L:

$$\langle I_{tot} \rangle(\theta) = I_A + \sum_{i \neq j} f_i f_j^* \frac{\sin(q R_{ij})}{q R_{ij}} \qquad (30)$$

where q and R_{ij} are the moduli of q and R_{ij}, respectively. It is interesting to note that the molecular interference term does not vanish after the average, as pointed out by Fano and Cohen in 1967 [152]. According to IAM, we can define the molecular contrast factor (MCF) as

$$\gamma = \frac{1}{I_A} \sum_{i \neq j} f_i f_j^* \frac{\sin(q R_{ij})}{q R_{ij}}. \qquad (31)$$

Next we consider the DCS extracted from the HATI spectra. The 'incident' electrons are 'generated' through tunnelling ionization. Thus, the 'incident' electron flux for each orientation angle is weighted by the tunnelling ionization rate $N(\Omega_L)$ which can be calculated using the MO-ADK theory. Thus the MCF for the DCS extracted from the HATI spectra of randomly distributed molecules is given by

$$\gamma = \frac{\sum_{i \neq j} f_i f_j^* \int e^{i q \cdot R_{ij}} N(\Omega_L) \, d\Omega_L}{\left(\sum_i |f_i|^2 \right) \int N(\Omega_L) \, d\Omega_L}. \qquad (32)$$

For isotropically distributed molecules, the MCF, γ, depends on the polar angle, θ, of the electrons only. If molecules are not isotropically distributed, the angular distributions of the molecules $\rho(\Omega_L)$ should be included in the average. In such a case, the DCS and γ will depend on both θ and φ where the two spherical angles are defined with respect to the polarization axis of the laser.

Can IAM be used for describing the elastic scattering that generates the HATI electrons? The returning electron energies are on the order of $3.2 U_p$. If 800 nm infrared lasers are used, the returning electron energy is about 35 eV if the peak intensity is 2×10^{14} W cm^{-2}. This is to be compared to tens to hundreds of keV used in GED. However, using mid-infrared (MIR) lasers of wavelength of say 1200 nm, the returning electron energy easily can reach about 100 eV. Can IAM work adequately at these energies? Since IAM neglects molecular bonding, if it is to work, it will have to be for hard collisions where electrons are backscattered to large angles.

Experimentally the DCS from randomly distributed molecules have been reported in earlier papers [153, 154]. In figures 26(a)–(d) we compare the measured DCS of CO_2 versus the prediction of IAM for incident electron energies of
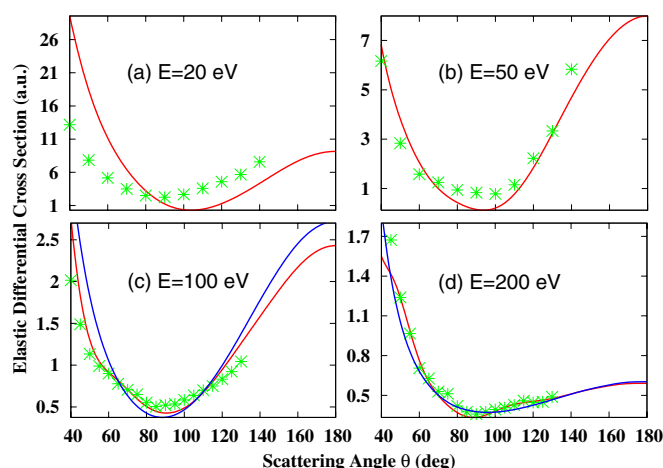
Figure 26. Elastic scattering cross sections at large angles between electrons and isotropically distributed CO_2 molecules. The experimental data [153, 154] are compared to the theoretical prediction of the independent atom model, showing poor agreement at 20 eV, but general good agreement at higher collision energies.

20, 50, 100 and 200 eV, respectively. It is clear that IAM does not work at 20 eV, but at above about 50 eV, the agreement between IAM and experiment becomes quite good. In figures 26(c) and (d) we also plot the incoherent sum of the DCS from the atoms, i.e. the I_A term. It shows that the minimum in the DCS is due to the minimum in the atomic DCS. Against the smooth atomic DCS, the molecular interference, i.e. the small oscillations in the total DCS against the smooth atomic DCS, can be clearly seen. As the interatomic separations increase, the oscillations will become more rapid.

There are no HATI spectra reported for molecular targets using MIR lasers to allow us to test the predictions of the IAM model yet. However, such experiments are being carried out at a number of laboratories [155]. In the immediate future, it would be desirable to measure HATI spectra for isotropically distributed molecules, and also for aligned molecules—just for molecules at equilibrium configurations, using MIR lasers. These data would allow us to check the validity region of the IAM model and to test how accurately the target structure can be retrieved from HATI spectra using laboratory MIR lasers.

4. Time-resolved dynamic chemical imaging with few-cycle infrared laser pulses

4.1. Introduction

Imaging, or the determination of the structure of an object, has always occupied an essential role in physical, chemical and biological sciences. For microscopic objects, x-ray diffraction and electron diffraction are the established means for achieving spatial resolution on the order of Ångstroms or less. These methods have been around for nearly half a century. However, they are not suitable for probing the structure of a dynamic system that evolves faster than a few picoseconds or so. Although ultrafast electron diffraction (UED) [156–158] and free-electron x-ray lasers that are just now coming online have the same goal of imaging dynamic systems, it is important

to investigate the potential of using small-scale laboratory infrared or MIR lasers for dynamic imaging of molecules. To develop such a method into practical tools, the theoretical foundation for the structure retrieval has to be established first.

In conventional GED for gas phase molecules, the radial distribution function of atoms in the molecules can be obtained by taking the inverse sine transform of the electron diffraction spectra from randomly distributed molecules [142, 149, 151]. This is similar to the x-ray diffraction method where the structure is obtained from an inverse Fourier transform. The retrieval, or the inverse scattering theory, for both methods are very simple. In practice, in modern electron diffraction of gaseous molecules [151], the structure retrieval is often aided by incorporating calculated parameters as if they were additional experimental data [159]. If molecules can be aligned or oriented, clearly, not only the interatomic distances can be determined but also the bond angles [160] in the molecule. Gas phase molecules can be aligned either by photodissociation with femtosecond laser pulses or by active laser alignment techniques [108, 161–163]. Today, infrared or MIR lasers with a pulse duration less than 10 fs are readily available. If these lasers can also be used for spatial imaging, then they can be developed into practical tools for dynamic imaging of transient molecules. Since the last step of the generation of HATI spectra is elastic scattering, similar to the scattering of molecules by a laboratory-prepared electron beam, we may look at whether it is possible to apply the same idea used in GED for imaging molecules with laser-induced returning electrons. In figure 26, we have shown that beginning at 50–100 eV, the DCS at large scattering angles are well described by the independent atom model. For a dynamic system, the composition of atoms in a molecule is already known. If the molecules undergo transformation and the DCS are measured at different times, can one retrieve the bond lengths and bond angles as the molecules evolve in time? The retrieval algorithm is not the inverse sine transform or Fourier transform as in GED or x-ray diffraction, respectively. At this time we use a genetic algorithm for the retrieval which has been tested for atomic targets already, as seen in the next subsection. More advanced methods may be used in the future.

4.2. Retrieving atomic structure parameters from HATI spectra of atoms

In section 2.4.1, we showed that accurate DCS can be extracted from the HATI spectra of atoms generated by Ti-sapphire lasers. If the DCS is available from experimental measurement, can one identify which target atom it is from? This question was addressed in [164] for rare gas atoms. For this purpose, each atom is modelled by an electron in a potential, parametrized in the form

$$V(r; \boldsymbol{a}) = -\frac{(1 + a_1 e^{-a_2 r} + a_3 r e^{-a_4 r} + a_5 e^{-a_6 r})}{r}. \quad (33)$$

Such a simple potential is often used to describe an atom within the single active electron approximation. The parameters are chosen such that the potential generates correct energies of the ground and the first few singly excited states of the atom. Note that for an atom with nuclear charge z, the potential at small r

is $-Z/r$. This imposes the condition $1+a_1+a_3+a_5 = Z$ on the parameters in equation (33). In using a genetic algorithm (GA) to find these parameters, this condition will not be imposed.

For the retrieval, we ask that if the elastic DCS are available experimentally at a few incident energies in the angular range from $120°$ to $180°$, will we be able to use GA to find the parameters a_i for $i = 1$–6 in equation (33) such that it allows us to find out from which atom the DCS came from? In [164], the DCS were generated first from a given model potential. By introducing a random error of $\pm 10\%$ to the DCS calculated, such data were treated as 'experimental results'. Using a GA [165], we looked for the set of a_i that would give best fit to the 'experimental' DCS. The fitness function is defined to be the mean square error of the 'experimental' DCS and the DCS calculated from the parametrized model potential. From the fitted set of a_i, the value $1+a_1+a_3+a_5$ was calculated and its value is used to identify the total charge z of the atom. One can further use the retrieved potential to calculate the binding energies of the ground state and first few excited states to show that they agree with the data generated from the input potential. More recently, in [166], actual experimental DCS extracted from the HATI spectra of [53] were used for the retrieval of the model potential for rare gas atoms. Both exercises demonstrated that it is relatively straightforward to identify the target atom when the theory for calculating elastic differential scattering cross sections is simple, and if the DCS for large scattering angles are available.

4.3. Retrieving molecular structure parameters from HATI spectra of molecules

Before illustrating the potential of using a GA to retrieve the molecular structure, we first examine how sensitively the DCS depend on interatomic separations. Consider isotropically distributed N_2. The equilibrium distance of this molecule is $R_0 = 2.06$ au. Take the returning electron energy of 100 eV, which can be readily achieved using 1200 nm MIR lasers. We use the IAM to calculate the DCS and obtain the molecular contrast factor γ, see equation (31). In figure 27(a) we show the γ for the angular range of 60–180°, by increasing or decreasing R from R_0 by 10% and 20%, respectively. One can see that γ changes quite rapidly with the value of R, meaning that the DCS is very sensitive to the change of interatomic distances. In figure 27(b) the γ for O_2 at the same scattering energy is shown. It also shows the same sensitivity as in figure 27(a). This sensitivity is not surprising. According to the IAM, the interatomic separations appear in equation (29) in the phase. From the perspective of dynamic imaging, the atomic composition of the molecule is known, and precise values of interatomic separations at the equilibrium configuration can be determined by other methods. Thus, the γ at R_0 is readily available. As the geometry of the molecule changes, the γ will evolve accordingly. For dynamic imaging, our first goal is to use the new γ to retrieve the new $\mathbf{R}_{i,j}$, i.e. the vectors connecting each pair of atoms in the molecule. In a typical chemical reaction, only a few atoms will change their positions significantly. Thus, the number of new interatomic separations to be retrieved in a dynamic system is limited.
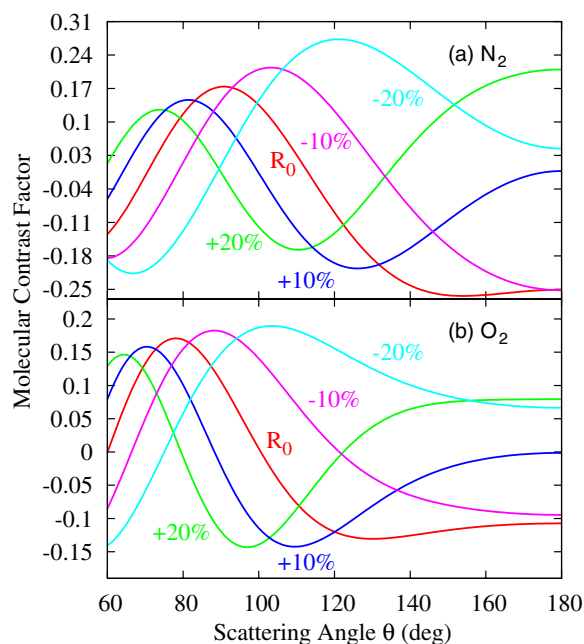

Figure 27. Simulation of the molecular contrast factor (see equation (32)) for the elastic differential scattering cross sections extracted from the HATI spectra. Comparisons are made for molecules at their normal equilibrium distances (R_0) and at interatomic distances increased or decreased by 10% and 20%, respectively. Note that $R_0 = 2.27$ for N_2 and 2.19 for O_2.

We mention that curves like in figure 27 can be obtained for different returning electron energies (by using different laser intensities or wavelengths), thus providing a large set of data that can be used for retrieving a small number of parameters. As in GED, if the molecules are not aligned, we can expect that only the radial distributions can be accurately retrieved. If the molecules are aligned, then both bond lengths and bond angles can be retrieved.

To 'reconstruct' such a retrieval process, we first simulate a fictitious scenario of the isomerization of HCN to CNH. For simplicity, we assume that the C-N bond length is fixed, but the position of H will change with time. We artificially move H to several positions, as shown in figure 28. We assume that H stays in the plane shown and that the polarization of the probe laser is perpendicular to this plane. Using the arbitrarily assigned positions of H, we calculated the DCS that can be extracted from the 'HATI' spectra. Using different initial search conditions, we use a GA to retrieve the position of H for each set of the DCS extracted from the HATI spectra. As shown in figure 28, the retrieved positions agree well with the input positions assumed.

In another exercise, in figure 29, we consider a model of a planar 3-fluoroiodobenzene molecule. The goal here is to identify the position of iodine and fluorine atoms. Assuming that both I and F do not stay at their equilibrium positions, but each at the distance and angle depicted in the figure. This is a simple example where five parameters are to be retrieved using a GA, the fifth parameter being the position of F and I with respect to the six carbons that they are to attach. We assume that laser polarization is perpendicular to the plane shown and the DCS can be extracted from the HATI spectra. This exercise
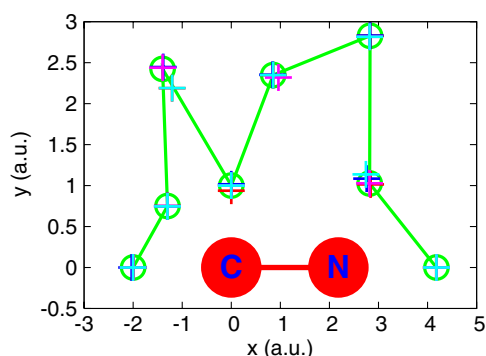
Figure 28. Simulation of dynamic structure retrieval using HATI momentum spectra for the isomerization of HCN to CNH. The positions of H were chosen in an arbitrary fashion indicated in the figure as the time evolves. In the model, the plane of the molecule is fixed perpendicular to the laser polarization direction. The assumed starting positions are given by circles. The retrieved positions in two different tries by a GA are shown by crosses.
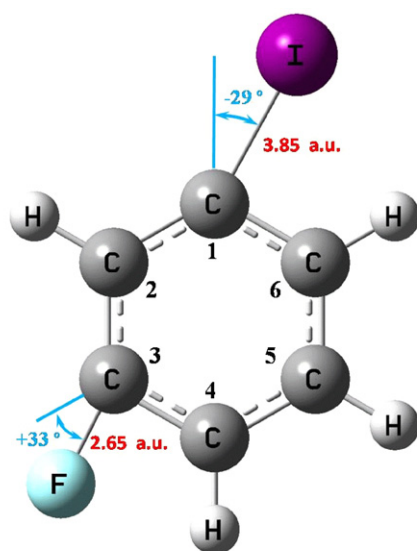
	ordering	(d_{CI}, θ_I)	(d_{CF}, θ_F)
"real" value	IHFHHH	$(3.85, -29.00°)$	$(2.65, +33.00°)$
Best fit	IHFHHH	$(3.83, -28.12°)$	$(2.65, +30.00°)$

Figure 29. A model of 3-fluoroiodobenzene away from its equilibrium configuration. We assume that the iodine and fluorine atoms are at the positions indicated. From the 'measured' HATI spectra, using the GA code, the order of iodine and fluorine atoms along the benzene ring as well as their bond lengths and bond angles retrieved using the GA code are shown in the table, and compared to the input values.

shows that if the IAM can be used to describe the DCS, then the retrieval of the five parameters is rather straightforward, see the table in figure 29. The accuracy of the retrieval can be improved with additional data from different laser intensities, wavelengths, as well as polarization directions. We comment that in dynamic chemical imaging the required accuracy for the retrieved parameters is not as high as the accuracy required in GED. The goal is to know the position of each atom at the intermediate time steps. For such dynamic processes, spatial

resolution of a few per cents is definitely adequate for the purpose of identifying the reaction pathway.

The exercises presented in this subsection show that the retrieval of atomic positions in a molecule from HATI spectra is rather simple if IAM is an adequate theory for describing elastic DCS at large angles. Even if the molecules are only partially aligned or oriented, the retrieval is expected to be robust. Clearly, further development of this model has to wait for the arrival of experimental HATI spectra using MIR lasers.

4.4. Other means and issues of probing molecular structure using strong fields

Until now, studies in strong-field physics have successfully provided some partial information on the structure of a molecule. For example, it has been well established that the orbital symmetry of the HOMO is accurately revealed in the alignment-dependent total tunnelling ionization rates. The alignment dependence of photoelectrons in the direction of laser polarization would also reveal the same information [167]. Despite the reported success of retrieving the HOMO wavefunction in N_2 [19], the tomographic method is not built on an accurate theory for HHG; thus, the retrieved result is not expected to be valid in general. Using QRS, an accurate theory for HHG and HATI spectra is available. However, the extracted PICS from HHG depends on the detailed molecular structure and a sophisticated theory for its accurate description. This is also true for the DCS extracted from the HATI spectra if the returning electron energy is low, say below 50 eV. At such low energies, molecular binding can still affect elastic scattering at large angles. Only at higher returning electron energies and large scattering angles will the electrons be scattered from the atomic centres where the DCS can be described by IAM. This is the condition where the retrieval of bond length and bond angles of a molecule becomes simple.

Clearly, knowing the positions of all the atoms in a molecule does not imply a full understanding of a dynamic chemical system. With known atomic positions in a molecule, however, quantum chemistry package can be used to calculate the dynamics of the molecule. For example, if the HHG spectra are also measured for a dynamic system, such data may be used to help identifying the electronic states involved in the reaction at a given time. In figure 30, we summarize what we perceive as a possible roadmap for the time-resolved chemical imaging based on strong-field rescattering physics. In this example, we assume that acetylene evolves along the potential surface depicted by the yellow curve [21], with intermediate configurations shown, and ends up as vinylidene. If a pump pulse is used to initiate the isomerization, a probe MIR laser can be used at different time delays to take the HATI spectra and the HHG spectra. Using QRS, the DCS for each time step can be extracted. Based on the IAM model, the positions of all the atoms in the molecule can then be retrieved. With such information, quantum chemistry codes, together with QRS, can be used to generate the HHG spectra. The calculated spectra can then be compared to the measured HHG spectra to check the retrieved molecular structure parameters, as well as the electronic states involved in the reaction. Clearly, to fully

Schematic of dynamic chemical imaging
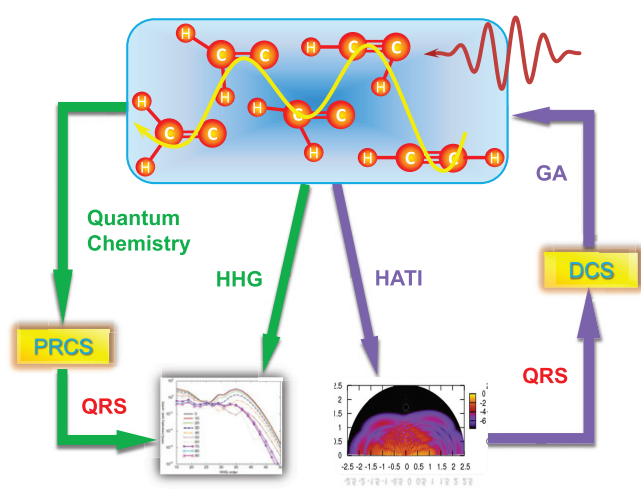
Figure 30. A close-loop module of dynamic chemical imaging of the isomerization of acetylene to vinylidene using strong MIR laser fields. The retrieval of the structure follows the direction of the arrows. See the text.

understand the dynamics of a transient molecule it will take many different measurements to fully describe the reaction pathways, but the identification of the configuration of all the atoms in the molecule, especially those which undergo large changes, is the very first step of such an effort.

Before closing we comment that for small molecular systems or systems that are relatively well studied, dynamic structural changes can also be probed using the Coulomb explosion [168, 169] or by measuring photoelectron spectra [170, 171]. For the latter, the probe pulse has to be relatively long (about hundreds of femtoseconds) since photoelectrons are used to identify the electronic states from which they came.

5. Summary and challenges ahead

In this review, we demonstrated that strong-field rescattering phenomena, such as high-energy ATI (HATI) electrons, high-order harmonic generation (HHG) and nonsequential double ionization (NSDI), can all be accurately described using the recently developed quantitative rescattering theory (QRS). According to QRS, electrons that return to recollide with the target ion are represented by an electron wave packet $W(k_r)$. This $W(k_r)$, to a high degree of accuracy, depends only on the property of the laser used, such as its wavelength, intensity, pulse duration and carrier-envelope phase, but not on the target. The HATI spectra are obtained by multiplying $W(k_r)$ with *field-free* differential elastic scattering cross sections between electrons and parent ions. Similarly, the HHG and NSDI spectra are obtained by multiplying $W(k_r)$ with *field-free* photo-recombination cross section and electron-impact ionization cross section, respectively. The nonlinear strong field enters only in $W(k_r)$, which can be calculated using the familiar simple strong-field approximation. The electron-ion collisions, such as elastic scattering, photo-recombination

and electron-impact ionization, are the standard processes that have been studied in the conventional energy domain collision physics. Advanced theoretical tools developed in the last five decades can be used directly for studying the rescattering phenomena.

The QRS model simplifies the interpretation of rescattering phenomena and provides accurate methods for performing quantitative calculations. In terms of probing the target structure, from time to time people may 'argue' that there is no new information in such time-domain measurements. However, recall that the returning electron wave packet $W(k_r)$ is a coherent electron source. Thus, laser-induced rescattering probes coherence properties that have not been investigated in energy domain measurements. For example, the phases of the high-order harmonics furnish the energy dependence of the phase of the transition dipole matrix element that is not available from photoionization measurements. Besides the HHG, the broad bandwidth and the coherent nature of the returning electron wave packet offer opportunities of studying and manipulating scattering phenomena that have not been fully exploited so far.

The QRS theory stresses that accurate *field-free* electron-ion scattering and recombination cross sections can be factored out from the HATI and the HHG spectra, respectively, and the results should be independent of the lasers used. Since elastic differential cross sections (DCS) between electrons and molecules are the well-tested method of gaseous electron diffraction (GED) for studying the structure of a molecule, we further explored the feasibility of using HATI electrons for imaging the structure of molecules. Preliminary studies show that HATI electron spectra, which are due to large-angle elastic scattering between the returning electrons and the molecular ion, can be well described using the independent atom model (IAM) even for electron energies as low as about 50–100 eV. These energies can be easily reached with mid-infrared lasers and they are already available. Since such lasers can be used to align molecules as well, alignment-dependent DCS can be extracted from the alignment-dependent HATI spectra. From alignment-dependent DCS one can retrieve the bond lengths *and bond angles* of atomic pairs in a molecule, a feat which still cannot be carried out with GED in general.

The potential of using strong fields for imaging molecular structure has not been seriously explored experimentally so far. In the very near future, HATI spectra from impulsively aligned molecules should be first studied experimentally using MIR lasers to demonstrate the feasibility of extracting bond lengths and bond angles of a nonlinear molecule. Since infrared or MIR lasers of duration of sub-ten femtoseconds are already available today, in the not-too-far future one can further explore this method as a competing tool for dynamic imaging of transient molecules. Clearly the potential is there, but more theoretical effort and experimental issues must be seriously addressed further, especially for dynamic systems.

References

[1] Corkum P B and Krausz F 2007 *Nature Phys.* **3** 381–7
[2] Agostini P and DiMauro L F 2004 *Rep. Prog. Phys.* **67** 813
[3] Chang Z, Rundquist A, Wang H, Murnane M M and Kapteyn H C 1997 *Phys. Rev. Lett.* **79** 2967
[4] Krausz F and Ivanov M 2009 *Rev. Mod. Phys.* **81** 163
[5] Remetter T *et al* 2006 *Nature Phys.* **2** 323
[6] Yang B, Schafer K J, Walker B, Kulander K C, Agostini P and DiMauro L F 1993 *Phys. Rev. Lett.* **71** 3770
[7] Gaarde M B, Schafer K J, Kulander K C, Sheehy B, Kim D and DiMauro L F 2000 *Phys. Rev. Lett.* **84** 2822
[8] Walker B, Sheehy B, Kulander K C and DiMauro L F 1996 *Phys. Rev. Lett.* **77** 5031
[9] L'Huillier A, Lompre L A, Mainfray G and Manus C 1983 *Phys. Rev.* A **27** 2503
[10] Larochelle S, Talebpour A and Chin S L 1998 *J. Phys. B: At. Mol. Opt. Phys.* **31** 1201
[11] Corkum P B 1993 *Phys. Rev. Lett.* **71** 1994
[12] Krause J L, Schafer K J and Kulander K C 1993 *Phys. Rev. Lett.* **68** 3535
[13] Morishita T, Le A T, Chen Z J and Lin C D 2008 *New J. Phys.* **10** 025011
[14] Lein M 2007 *J. Phys. B: At. Mol. Opt. Phys.* **40** R135
[15] Zou T, Bandrauk A D and Corkum P B 1996 *Chem. Phys. Lett.* **259** 313–20
[16] Hu S X and Collins L A 2005 *Phys. Rev. Lett.* **94** 073004
[17] Spanner M, Smirnova O, Corkum P B and Ivanov M 2004 *J. Phys. B: At. Mol. Opt. Phys.* **37** L243
[18] Yurchenko S N, Patchkovskii S, Litvinyuk I V, Corkum P B and Yudin G L 2004 *Phys. Rev. Lett.* **93** 223003
[19] Itatani J, Levesque J, Zeidler D, Niikura H, Pepen H, Kiefer J C, Corkum P B and Villeneuve D M 2004 *Nature* **432** 867
[20] Levesque J, Zeidler D, Marangos J P, Corkum P B and Villeneuve D M 2007 *Phys. Rev. Lett.* **98** 183903
[21] Le V H, Le A T, Xie R H and Lin C D 2007 *Phys. Rev.* A **76** 013414
[22] Schmidt M W *et al* 1993 *J. Comput. Chem.* **14** 1347
[23] Frisch M J *et al* 2003 *GAUSSIAN 03* revision C.02 (Gaussian Inc., Pittsburgh, PA)
[24] Werner H-J *et al* 2003 *MOLPRO* version 202.6: a package of *ab initio* programs (Birmingham, UK)
[25] Fienup J R 1982 *Appl. Opt.* **21** 2758
[26] Miao J, Charalambous C, Kirz H and Sayre D 1999 *Nature* **400** 342
[27] Lewenstein M, Balcou Ph, Ivanov M Yu, L'Huillier A and Corkum P B 1994 *Phys. Rev.* A **49** 2117
[28] Paulus G G, Becker W, Nicklich W and Walther H 1994 *J. Phys. B: At. Mol. Opt. Phys.* **27** L703
[29] Becker W *et al* 2002 *Adv. At. Mol. Opt. Phys.* **48** 35
[30] Hasovic E, Busuladžić M, Gazibegović-Busuladžić A, Milošević D B and Becker W 2007 *Laser Phys.* **17** 376
[31] Lewenstein M, Kulander K C, Schafer K J and Bucksbaum P H 1995 *Phys. Rev.* A **51** 1495
[32] Chen Z J, Morishita T, Le A T and Lin C D 2007 *Phys. Rev.* A **76** 043402
[33] Tong X M, Watahiki S, Hino K and Toshima N 2007 *Phys. Rev. Lett.* **99** 093001
[34] Morishita T, Le A T, Chen Z J and Lin C D 2008 *Phys. Rev. Lett.* **100** 013903
[35] Chen Z J, Le A T, Morishita T and Lin C D 2009 *Phys. Rev.* A **79** 033409
[36] Le A T, Lucchese R R, Tonzani S, Morishita T and Lin C D 2009 *Phys. Rev.* A **80** 013401
[37] Micheau S, Chen Z J, Le A T and Lin C D 2009 *Phys. Rev.* A **79** 013417
[38] Agostini P, Fabre F, Mainfray G, Petite G and Rahman N K 1979 *Phys. Rev. Lett.* **42** 1127
[39] L'Huillier A, Lompre L A, Mainfray G and Manus C 1983 *Phys. Rev.* A **27** 2503
[40] Schafer K J, Yang B, DiMauro L F and Kulander K C 1993 *Phys. Rev. Lett.* **70** 1599
[41] Muller H G 1999 *Phys. Rev.* A **60** 1341
[42] Chen Z J, Morishita T, Le A T, Wickenhauser M, Tong X M and Lin C D 2006 *Phys. Rev.* A **74** 053405
[43] Morishita T, Chen Z, Watanabe S and Lin C D 2007 *Phys. Rev.* A **75** 023407
[44] Tong X M and Lin C D 2005 *J. Phys. B: At. Mol. Opt. Phys.* **38** 2593
[45] Augst S, Meyerhofer D D, Strickland D and Chin S L 1991 *J. Opt. Soc. Am.* B **8** 858
[46] Zhou X X, Tong X M, Zhao Z X and Lin C D 2005 *Phys. Rev.* A **71** 061801
[47] Zhou X X, Tong X M, Zhao Z X and Lin C D 2005 *Phys. Rev.* A **72** 033412
[48] Le A T, Tong X M and Lin C D 2006 *Phys. Rev.* A **73** 041402
[49] Schiff L I 1968 *Quantum Mechanics* 3rd edn (New York: McGraw-Hill) p 145
[50] Chen Z J, Le A T, Morishita T and Lin C D 2009 *J. Phys. B: At. Mol. Opt. Phys.* **42** 061001
[51] Kling M F, Rauschenberger J, Verhoef A J, Hasović E, Uphues T, Milošević D B, Muller H G and Vrakking M J J 2008 *New J. Phys.* **10** 025024
[52] Ray D *et al* 2008 *Phys. Rev. Lett.* **100** 143002
[53] Okunishi M, Morishita T, Prümper G, Shimada K, Lin C D, Watanabe S and Ueda K 2008 *Phys. Rev. Lett.* **100** 143001
[54] Colosimo P *et al* 2008 *Nature Phys.* **4** 386
[55] Paulus G G, Lindner F, Walther H, Baltuška A, Goulielmakis E, Lezius M and Krausz F 2003 *Phys. Rev. Lett.* **91** 253004
[56] Abel M J, Pfeifer T, Aurélie J, Nagel P M, Bell M J, Neumark D M and Leone S R 2009 *J. Phys. B: At. Mol. Opt. Phys.* **42** 075601
[57] Tong X M, Hino K and Toshima N 2006 *Phys. Rev.* A **74** 031405
[58] Liu X *et al* 2004 *Phys. Rev. Lett.* **93** 263001
[59] Kling M F *et al* 2006 *Science* **312** 246
[60] Znakovskaya I, von Hoff P, Zherebtsov S, Wirth A, Herrwerth O, Vrakking M J, de Vivie-Riedle R and Kling M F 2009 *Phys. Rev. Lett.* **103** 103002
[61] Tong X M and Lin C D 2007 *Phys. Rev. Lett.* **98** 123002
[62] Tong X M and Lin C D 2007 *J. Phys. B: At. Mol. Opt. Phys.* **40** 641
[63] Gräfe S and Ivanov M Yu 2007 *Phys. Rev. Lett.* **99** 163603
[64] Hentschel M, Kienberger R, Spielmann C, Reider G A, Milosevic N, Brabec T, Corkum P, Heinzmann U, Drescher M and Krausz F 2001 *Nature (London)* **414** 509
[65] Feng X, Gilbertson S, Mashiko H, Wang H, Khan S D, Chini M, Wu Y, Zhao K and Chang Z 2009 *Phys. Rev. Lett.* **103** 183901
[66] Sansone G *et al* 2006 *Science* **314** 443
[67] Haworth C A, Chipperfield L E, Robinson J S, Knight P L, Marangos J P and Tisch J W G 2007 *Nature Phys.* **3** 52
[68] Chen Z J, Wittmann T, Horvath B and Lin C D 2009 *Phys. Rev.* A **80** 061402
[69] Micheau S, Chen Z J, Le A T, Rauschenberger J, Kling M F and Lin C D 2009 *Phys. Rev. Lett.* **102** 073001

J. Phys. B: At. Mol. Opt. Phys. **43** (2010) 122001

Topical Review

[70] Wittmann T, Horvath B, Helml W, Schätzel M G, Gu X, Cavalieri A L, Paulus G G and Kienberger R 2009 *Nature Phys.* **5** 357

[71] Chen Z J, Liang Y Q and Lin C D 2010 *Phys. Rev. Lett.* in press

[72] Lotz W 1968 *Z. Phys.* **216** 241

[73] Guo C, Li M, Nibarger J P and Gibson G N 1998 *Phys. Rev.* A **58** R4271

[74] Staudte A *et al* 2007 *Phys. Rev. Lett.* **99** 263002

[75] Rudenko A, de Jesus V L B, Ergler Th, Zrost K, Feuerstein B, Schröter C D, Moshammer R and Ullrich J 2007 *Phys. Rev. Lett.* **99** 263003

[76] Feuerstein B *et al* 2001 *Phys. Rev. Lett.* **87** 043003

[77] Le A T, Morishita T and Lin C D 2008 *Phys. Rev.* A **78** 023814

[78] Cooper J W 1962 *Phys. Rev.* **128** 681

[79] Mairesse Y *et al* 2003 *Science* **302** 1540

[80] Gaarde M B, Tate J L and Schafer K J 2008 *J. Phys. B: At. Mol. Opt. Phys.* **41** 132001

[81] Jin C, Le A T and Lin C D 2009 *Phys. Rev.* A **79** 053413

[82] Popmintchev T, Chen M C, Bahabad A, Gerrity M, Sidorenko P, Cohen O, Christov I P, Murnane M M and Kapteyn H C 2009 *Proc. Natl Acad. Sci.* **106** 10516

[83] Tosa V, Balogh E and Kovács K 2009 *Phys. Rev.* A **80** 045801

[84] Doumy G, Wheeler J, Roedig C, Chirla R, Agostini P and DiMauro L F 2009 *Phys. Rev. Lett.* **102** 093002

[85] Minemoto S, Umegaki T, Oguchi Y, Morishita T, Le A T, Watanabe S and Sakai H 2008 *Phys. Rev.* A **78** 061402

[86] Woerner H J, Niikura H, Bertrand J B, Corkum P B and Villeneuve D M 2009 *Phys. Rev. Lett.* **102** 103901

[87] Woerner H J 2010 private communication

[88] Samson J A R and Stolte W C 2002 *J. Electron Spectrosc. Relat. Phenom.* **123** 265

[89] Frolov M V, Manakov N L, Sarantseva T S and Starace A F 2009 *J. Phys. B: At. Mol. Opt. Phys.* **42** 035601

[90] Frolov M V, Manakov N L and Starace A F 2009 *Phys. Rev.* A **79** 033406

[91] Cerkic A, Hasovic E, Milosevic D B and Becker W 2009 *Phys. Rev.* A **79** 033413

[92] Tolstikhin O I, Morishita T and Watanabe S 2010 *Phys. Rev.* A **81** 033415

[93] Lein M, Corso P P, Marangos J P and Knight P L 2003 *Phys. Rev.* A **67** 023819

[94] Telnov D A and Chu S I 2007 *Phys. Rev.* A **76** 043412

[95] Kamta G L and Bandrauk A D 2005 *Phys. Rev.* A **71** 053407

[96] Le A T, Picca R D, Fainstein P D, Telnov D A, Lein M and Lin C D 2008 *J. Phys. B: At. Mol. Opt. Phys.* **41** 081002

[97] Kanai T, Minemoto S and Sakai H 2005 *Nature* **435** 470

[98] Vozzi C, Calegari F, Benedetti E, Caumes J-P, Sansone G, Stagira S and Nisoli M 2005 *Phys. Rev. Lett.* **95** 153902

[99] Wagner N, Zhou X, Lock R, Li W, Wüest A, Murnane M and Kapteyn H C 2007 *Phys. Rev.* A **76** 061403

[100] Kanai T, Takahashi E J, Nabekawa Y and Midorikawa K 2008 *Phys. Rev.* A **77** 041402

[101] Zhou X, Lock R, Li W, Wagner N, Murnane M M and Kapteyn H C 2008 *Phys. Rev. Lett.* **100** 073902

[102] Boutu W *et al* 2008 *Nature Phys.* **4** 545

[103] Tong X M, Zhao Z X and Lin C D 2002 *Phys. Rev.* A **66** 033402

[104] Zhao S F, Jin C, Le A T, Jiang T F and Lin C D 2010 *Phys. Rev.* A **81** 033423

[105] Stolow A and Underwood J G 2008 *Adv. Chem. Phys.* **139** 497

[106] Reid K L 2003 *Annu. Rev. Phys. Chem.* **54** 397

[107] Lucchese R R, Raseev G and McKoy V 1982 *Phys. Rev.* A **25** 2572

[108] Stapelfeldt H and Seideman T 2003 *Rev. Mod. Phys.* **75** 543

[109] Stratmann R E and Lucchese R R 1995 *J. Chem. Phys.* **102** 8493

[110] Bandarage G and Lucchese R R 1993 *Phys. Rev.* A **47** 1989

[111] Stratmann R E, Zurales R W and Lucchese R R 1996 *J. Chem. Phys.* **104** 6482

[112] Lein M, Hay N, Velotta R, Marangos J P and Knight P L 2002 *Phys. Rev. Lett.* **88** 183903

[113] Smirnova O, Mairesse Y, Patchkovskii S, Dudovich N, Villeneuve D, Corkum P and Ivanov M Yu 2009 *Nature* **460** 972

[114] Smirnova O, Patchkovskii S, Mairesse Y, Dudovich N, Villeneuve D, Corkum P and Ivanov M Yu 2009 *Phys. Rev. Lett.* **102** 063601

[115] Smirnova O, Patchkovskii S, Mairesse Y, Dudovich N and Ivanov M Yu 2009 *Proc. Natl Acad. Sci. USA* **106** 16556

[116] Le A T, Tong X M and Lin C D 2007 *J. Mod. Opt.* **54** 967

[117] Abdurrouf A and Faisal F H M 2009 *Phys. Rev.* A **79** 023405

[118] Zhao S F, Jin C, Le A T, Jiang T F and Lin C D 2009 *Phys. Rev.* A **80** 051402

[119] Son S K and Chu S I 2009 *Phys. Rev.* A **80** 011403

[120] Abu-samha M and Madsen L B 2009 *Phys. Rev.* A **80** 023401

[121] Pavičić D, Lee Kevin F, Rayner D M, Corkum P B and Villeneuve D M 2007 *Phys. Rev. Lett.* **98** 243001

[122] Thomann I, Lock R, Sharma V, Gagnon E, Pratt S T, Kapteyn H C, Murnane M M and Li W 2008 *J. Phys. Chem.* A **112** 9382

[123] Spanner M and Patchkovskii S 2009 *Phys. Rev.* A **80** 063411

[124] Le A T, Lucchese R R, Lee M T and Lin C D 2009 *Phys. Rev. Lett.* **102** 203001

[125] Lein M, Hay N, Velotta R, Marangos J P and Knight P L 2002 *Phys. Rev. Lett.* **88** 183903

[126] Kaku M, Masuda K and Miyazaki K 2004 *Japan. J. Appl. Phys.* **43** L591

[127] Itatani J, Zeidler D, Levesque J, Spanner M, Villeneuve D M and Corkum P B 2005 *Phys. Rev. Lett.* **94** 123902

[128] Mairesse Y, Levesque J, Dudovich N, Corkum P B and Villeneuve D M 2008 *J. Mod. Opt.* **55** 2591

[129] McFarland B K, Farrell J P, Bucksbaum P H and Gühr M 2008 *Science* **322** 1232

[130] Le A T, Lucchese R R and Lin C D 2009 *J. Phys. B: At. Mol. Opt. Phys.* **42** 21100

[131] Lein M, De Nalda R, Heesel E, Hay N, Springate E, Velotta R, Castillejo M, Knight P L and Marangos J P 2005 *J. Mod. Opt.* **52** 465

[132] Mairesse Y *et al* 2008 *New J. Phys.* **10** 025028

[133] Lee G H, Kim I J, Park S B, Kim T K and Nam C H 2008 *Opt. Lett.* **33** 2083

[134] Zhou X, Lock R, Wagner N, Li W, Kapteyn H C and Murnane M M 2009 *Phys. Rev. Lett.* **102** 073902

[135] Le A T, Lucchese R R and Lin C D 2010 *Phys. Rev.* A (submitted) (arXiv:1002.3384v1)

[136] Ivanov M Yu, Brabec T and Burnett N 1996 *Phys. Rev.* A **54** 742

[137] Smirnova O, Spanner M and Ivanov M Yu 2008 *Phys. Rev.* A **77** 033407

[138] Okunishi M, Itaya R, Shimada K, Prümper G, Ueda K, Busuladžić M, Gazibegović-Busuladžić A, Milošević D B and Becker W 2008 *J. Phys. B: At. Mol. Opt. Phys.* **41** 21004

[139] Busuladžić M, Gazibegović-Busuladžić A, Milošević D B and Becker W 2008 *Phys. Rev. Lett.* **100** 203003

[140] Cornaggia C 2009 *J. Phys. B: At. Mol. Opt. Phys.* **42** 161002

[141] Meckel M *et al* 2008 *Science* **320** 1478

[142] Hargittai I and Hargittai M 1988 *Stereochemical Applications of Gas-Phase Electron Diffraction* (New York: VCH) and references therein

[143] Lane N F 1980 *Rev. Mod. Phys.* **52** 29

[144] Trajmar S, Chutjian A and Register D F 1983 *Phys. Rep.* **97** 220

[145] Morgan L A, Tennyson J and Gillan C J 1998 *Comput. Phys. Commun.* **114** 120

[146] Tonzani S and Greene C H 2006 *J. Chem. Phys.* **124** 054312

[147] Tonzani S 2007 *Comput. Phys. Commun.* **176** 146

[148] Harvey A G and Tennyson J 2009 *J. Phys. B: At. Mol. Opt. Phys.* **42** 095101

[149] Schäfer L 1976 *Appl. Spectrosc.* **30** 123

[150] McCaffrey P D, Dewhurst J K, Rankin D W H, Mawhorter R J and Sharma S 2008 *J. Chem. Phys.* **128** 204304

[151] Hinchley S, Wann D A and Rankin D W H 2005 *Int. J. Quantum. Chem.* **101** 878

[152] Cohen H D and Fano U 1966 *Phys. Rev.* **150** 30

[153] Register D F, Nishimura H and Trajmar S 1980 *J. Phys. B: At. Mol. Opt. Phys.* **13** 1651

[154] Iga I, Homem M G, Mazon K T and Lee M T 1999 *J. Phys. B: At. Mol. Opt. Phys.* **32** 4373

[155] DiMauro L 2010 private communication

[156] Zewail A H and Thomas J M 2009 *4D Electron Microscopy: Imaging in Space and Time* (London: Imperial College Press)

[157] Ihee H, Lobastov V A, Gomez U M, Goodson B M, Srinivasan R, Ruan C Y and Zewail A H 2001 *Science* **291** 458

[158] Siwick B J, Dwyer J R, Jordan R E and Miller D 2003 *Science* **302** 1382

[159] Mitzel N W and Rankin D W H 2003 *J. Chem. Soc., Dalton Trans.* 3650

[160] Williamson C and Zewail A H 1994 *J. Phys. Chem.* **98** 2766

[161] Reckenthaeler P, Centurion M, Fuß W, Trushin S A, Krausz F and Fill E E 2009 *Phys. Rev. Lett.* **102** 213001

[162] Spence J 2005 *J. Electron Microsc.* **54** 163

[163] Ryu S, Stratt R M and Weber P M 2003 *J. Phys. Chem.* A **107** 6622

[164] Xu J L, Zhou H L, Chen Z J and Lin C D 2009 *Phys. Rev.* A **79** 052508

[165] Carroll D L 1999 *FORTRAN genetic algorithm driver* http://cuaerospace.com/carroll/ga.html

[166] Morishita T, Umegaki T, Watanabe S and Lin C D 2009 *J. Phys.: Conf. Ser.* **194** 012011

[167] Staudte A *et al* 2009 *Phys. Rev. Lett.* **102** 033004

[168] Hishikawa A, Matsuda A, Fushitani M and Takahashi E J 2007 *Phys. Rev. Lett.* **99** 258302

[169] Xu H, Okino T and Yamanouchi K 2009 *J. Chem. Phys.* **131** 151102

[170] Bisgaard C Z, Clarkin O J, Wu G, Lee A M D, Geßner O, Hayden C C and Stolow A 2009 *Science* **323** 1464

[171] Strasser D, Goulay F and Leone S R 2007 *J. Chem. Phys.* **127** 184305